

Article

A PMSG Wind Energy System Featuring Low-Voltage Ride-through via Mode-Shift Control

Rania A. Ibrahim *  and Nahla E. Zakzouk

Electrical and Control Engineering Department, College of Engineering and Technology, Arab Academy for Science and Technology (AAST), Alexandria 1029, Egypt; nahlaezeldin@aast.edu

* Correspondence: rania_assem@aast.edu

Abstract: Low-voltage ride-through (LVRT) and grid support capability are becoming a necessity for grid-tied renewable energy sources to guarantee utility availability, quality and reliability. In this paper, a swap control scheme is proposed for grid-tied permanent magnet synchronous generator (PMSG) MW-level wind turbines. This scheme shifts system operation from maximum power point tracking (MPPT) mode to LVRT mode, during utility voltage sags. In this mode, the rectifier-boost machine-side converter overtakes DC-link voltage regulation independently of the grid-side converter. The latter attains grid synchronization by controlling active power injection into the grid to agree with grid current limits while supporting reactive power injection according to the sag depth. Thus grid code requirements are met and power converters safety is guaranteed. Moreover, the proposed approach uses the turbine-generator rotor inertia to store surplus energy during grid voltage dips; thus, there is no need for extra hardware storage devices. This proposed solution is applied on a converter topology featuring a minimal number of active switches, compared to the popular back-to-back converter topology. This adds to system compatibility, reducing its size, cost and switching losses. Simulation and experimental results are presented to validate the proposed approach during normal and LVRT operation.

Keywords: wind energy conversion systems (WECS); PMSG; LVRT; symmetrical voltage sag/dip; machine-side converter (MSC); grid-side converter (GSC); swap control; grid interface; reactive power control



Citation: Ibrahim, R.A.; Zakzouk, N.E. A PMSG Wind Energy System Featuring Low-Voltage Ride-through via Mode-Shift Control. *Appl. Sci.* **2022**, *12*, 964. <https://doi.org/10.3390/app12030964>

Academic Editors:

Cristian-Dragoş Dumitru,
Adrian Gligor, Gheorghe Grigoras
and Bogdan-Constantin Neagu

Received: 7 December 2021

Accepted: 13 January 2022

Published: 18 January 2022

Publisher's Note: MDPI stays neutral with regard to jurisdictional claims in published maps and institutional affiliations.



Copyright: © 2022 by the authors. Licensee MDPI, Basel, Switzerland. This article is an open access article distributed under the terms and conditions of the Creative Commons Attribution (CC BY) license (<https://creativecommons.org/licenses/by/4.0/>).

1. Introduction

Climate change due to carbon emissions is a true global issue that needs strict actions to reduce its threatening impacts. Shifting to renewables and transitioning to a low-carbon energy are implicit for a more sustainable and cleaner environment. Although reaching net zero emissions will demand serious measures by a large number of sectors and players, wind power is placed to be a keystone in accelerating the global energy transition as one of the fastest growing renewable energy technologies [1]. Despite the global pandemic, the world added a record of 93 GW of wind power capacity in 2020, representing an increase of almost 53% relative to 2019 installations and hitting a total global wind power capacity of 743 GW [2].

The doubly fed induction generator (DFIG)-based WECS has been a popular topology for medium-size turbines with a global market share. However, a new trend is directed for taller and larger wind turbines, such as PMSG-based ones, to extract more power and maximize energy captured via their associated full-scale converter systems [1]. This configuration aims to achieve balance between generator size and maintenance effort, where the need for a gearbox can be eliminated by using a high pole number-based PMSG [3,4]. A comparative study of DFIGs and PMSGs showed that during the machine early life, a PMSG has a failure rate 40% lower than that of a comparable DFIG [5]. With full-scale converters and the ability to operate across the full speed range, the system is

able to perform reactive power compensation and smooth grid connection. Moreover, the generator is fully decoupled from the grid, which adds to its robustness against utility faults. This makes the WECS better in terms of fault ride through compliance that can be achieved without any additional hardware devices. In addition, wind energy conversion efficiency is the highest compared to other types of turbines [6]. Finally, these systems can achieve higher power density with multiple generators and by using the distributed drive train concept [3]. To summarize, PMSG-based wind turbines have gained great attention on wind farms due to their gearless operation, smaller maintenance cost, high efficiency, as well as their full controllability range, which makes them more favorable than their counterpart.

Normally, WECS feature two power conversion stages that employ an AC/DC machine-side converter (MSC) at the generation end and a DC/AC grid-side converter (GSC) at the grid side. PMSG MSCs are full-scale power converters that must be rated the same as the generator capacity; thus, the system converter size, cost and complexity increase. Commonly, there are two types of MSCs: active front-end converters or passive front-end ones (diode rectifier) that can be assisted with a boost DC/DC converter. In an attempt to reduce the converter size and cost, passive front-end converter topology can be an attractive solution. It features less active switches and in turn less gate-drive circuits, reducing converter implementation and control complexity. Moreover, less switching losses are experienced, especially at low and average turbine speed conditions [7,8]. That is why, for low and medium power ranges, passive front-end converters are considered a predominant solution [9]. However, a trade-off for using this topology is met with higher torque ripples due to the uncontrolled nature of the generator stator currents [7,9,10].

The dramatic scale-up of wind energy penetration and integration to the electrical network result in several challenges in terms of utility, stability, and reliability. Consequently, revised grid codes urge wind power plants to maintain system continuity even under abnormal operation and transients. Among these challenges, LVRT capability has lately gained much attention as one of the main integration issues that have been standardized in many countries. An LVRT requirement implies that wind power plants must remain connected even in the presence of transient grid voltage dips. This maintains the network voltage and frequency stability by injecting active and reactive power into the grid under a predetermined profile related to the grid dip severity. Thus, LVRT is quite a challenging requirement, affecting the design and control of WECS power converters, for grid stability support and system reliability enhancement. Several studies have been conducted to investigate the performance of various LVRT techniques on various WECS during grid faults. Commonly, these techniques can be divided into hardware solutions or software ones (modified control-based methods), which will be presented in the following section [11–14].

In this paper, a PMSG-based MW-level WECS is considered, applying passive-end MSC to achieve an economic fault-tolerant system able to compromise between generator robustness against grid faults and converter cost-effectiveness. For LVRT, a swap feature modification is proposed for the classical control scheme, enabling it to successfully work during normal conditions or utility voltage sags. Normally at no fault, the MSC achieves MPPT while the GSC regulates the DC-link voltage by controlling the grid current to transfer the extracted active power to grid [15]. In this case, no reactive power (VAR) control is required. However, during grid faults, if the classical non-swap control is still applied, the GSC action will be affected as it is directly coupled to the grid. The GSC ability to control the DC voltage becomes limited, since it can no longer deliver the wind power extracted by the MSC to the grid. Consequently, the energy surplus must be dissipated into the system, causing DC-link over voltages and grid current increase [15]. Meanwhile, the GSC should satisfy grid requirements and inject VAR into the grid, as per the standards [16]. Thus, the GSC is required to achieve both functions of VAR control and DC-link voltage regulation simultaneously. Since both control loops have different dynamics and different

time constants, this will affect the VAR control response since DC-link voltage dynamics are slower due to the large DC-link capacitor size.

On the contrary, applying the proposed swap control action, system operation will be shifted from MPPT mode to LVRT mode. In this mode, the responsibility of DC-link voltage control is overtaken by the MSC rather than the GCS, which independently controls grid current to inject the suitable active and reactive power into the grid based on the sag depth. This increases the system capability of decoupling the grid current controller from the DC-link voltage controller during LVRT conditions since both controllers feature different time constants and dynamics. Moreover, this prevents any noise or power oscillation propagation from one controller to another. Any surplus energy is stored in the rotor inertia with no additional circuit required [13]. Finally, rises in inverter DC-link voltage and grid currents are eliminated, thus maintaining power converter safety and meeting system interconnection requirements. Compared to other alternative topologies in the literature [15,17–23], the proposed approach features these merits, albeit with a converter topology containing the minimum number of active switches. This in turn reduces converter switching losses and cost, simplifies its implementation and minimizes its control complexity. A simulation set-up is implemented along with an experimental correlated prototype to verify the effectiveness of the proposed swap technique.

This paper is divided into nine sections. Section 2 describes the LVRT capability and recent modified control-based mitigation studies. Section 3 describes the considered PMSG WECS configuration and model. In Section 4, the authors explain the proposed mode-shift LVRT control for grid faults. Section 5 depicts the simulation analysis of the studied system using MATLAB/Simulink software, while Section 6 verifies the results through experimental validation. A discussion is added in Section 7, along with a conclusion in Section 8, and finally prospective future work is outlined in Section 9.

2. Low-Voltage Ride-through Capability

As the capacity of grid-tied wind energy systems increased, such integration has encouraged power utility operators to revise grid codes and to include technical requirements of interconnected wind power plants to ensure grid stability and reliability. These rules vary from country to country, but they share some common requirements, such as LVRT capability, voltage and frequency variation limits, active power and frequency control, reactive power control, voltage regulation and power factor control [24]. As indicated previously, LVRT indicates the ability of a wind energy system to stay connected to the utility network for a short time during grid faults and at voltage dip instances to minimize any power generation losses. Different grid codes are tailored accordingly and vary in terms of voltage dip severity and the allowable operation time for wind turbines to remain connected to the network.

A typical LVRT curve is shown in Figure 1, with a special focus on the (E-ON) code, as set by the German Distribution and Distribution Utility operators [25]. In the presence of a grid dip, the wind turbine generators must remain connected to the utility network if the line voltage remains over the limit line in Figure 1a.

Besides satisfying the active power requirement, the WECS is required to inject reactive current as specified in Figure 1b without exceeding the current limit of the converter, in order to assist the utility in holding the grid voltage. The amount of reactive power to be injected depends on the amount of grid voltage dip, the amount of reactive current present before the dip occurrence and the rated grid current [16]. According to Figure 1b, LVRT capability should start when a voltage sag is detected below 90% of its nominal value. For voltage sags ranging between 50 and 90%, 2% reactive current needs to be provided for every 1% voltage dip. The WECS must be able to provide 100% reactive current if the grid voltage falls below 50% [26].

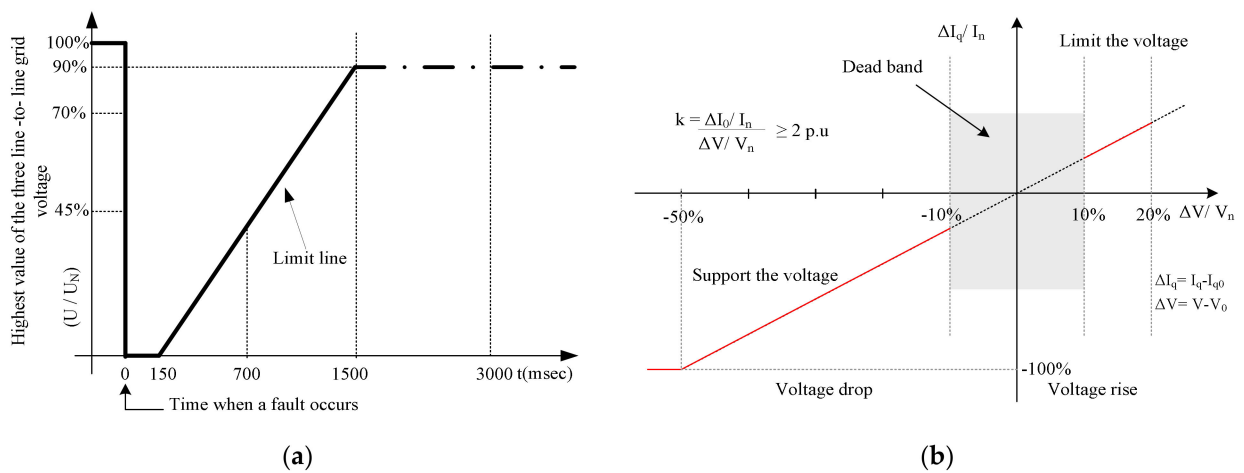


Figure 1. LVRT requirement: (a) voltage limit curves; (b) reactive current injection during fault.

As mentioned earlier, LVRT enhancement techniques for PMSG WECS are typically divided into types that rely on the control scheme modification and others that require auxiliary hardware modification. External hardware-based methods include chopper-controlled braking resistance [27], energy storage systems [28], fault current limiters [29] and using FACT devices at the point of common coupling (PCC) [30,31]. On the other hand, modified controller-based schemes rely on enhancing the applied control scheme to include pitch angle control [32,33], generator de-loading control [34], or reactive power control [7,13,35]. Hardware solutions usually feature less control complexity, yet with more size and cost compared to the alternative software control modifications. Thus, the latter is considered in this paper.

Table 1 presents the most recent modified control-based techniques introduced to address the LVRT problem facing grid-tied PMSG WECS [15,29–35]. It can be concluded that all presented techniques terminate the MPPT process during sag conditions to limit grid current rises and maintain its value within the safe limit as per grid standards. Additionally, during voltage sag, all techniques inject reactive power (VAR) into the grid as required by grid regulations except [17], which shows deficiency regarding VAR support. Coordinated control between both MSC and GSC for DC-link voltage control is achieved in [18]. Additional auxiliary hardware devices are required in [17,19–21] to store the excess power during sag conditions, which adds to system complexity and cost. Finally, [15,22,23] prevent any active power injection during faults, thus limiting WECS efficiency due to the loss of active power transferred to the grid during the sag.

Table 1. Recent LVRT mitigation techniques in grid-tied PMSG WECS.

| # | Topology + Switches Number | | Action of LVRT Mitigation Technique during Fault | Additional Devices | Mitigated Para |
|----------|--|---|---|---|--------------------------|
| | MSC | GSC | | | |
| [17] | Active front-end (AFER) for MPPT Active Sw.: 6 | AFER for V_{dc} control, grid interface Active Sw.: 6 | <ul style="list-style-type: none"> MPPT is perceived to keep I_g within safe limit. V_{dc} control is achieved by dissipating excess power in crowbar resistor. Grid synchronization is achieved by the GSC. No Q support. | Extra crowbar resistance is required | I_g rises |
| [22] | AFER for MPPT Active Sw.: 6 | AFER for V_{dc} control, grid interface and I_g control Active Sw.: 6 | <ul style="list-style-type: none"> MPPT is seized via MSC and P grid is decreased to keep I_g within safe limits. Grid synchronization and Q control is carried out by GSC for grid support. Surplus energy is stored in rotor inertia. | Not required | I_g and V_{dc} rises |
| [18] | AFER for MPPT Active Sw.: 6 | AFER for grid interface, I_g control and V_{dc} regulation Active Sw.: 6 | <ul style="list-style-type: none"> V_{dc} control is based on coordinated control between the MSC and GSC according to the GSC active power limit capability; GSC controls V_{dc}, and MSC works in MPPT mode. If the DC-link current is within the GSC active power capability limits, otherwise MSC and GSC will both control V_{dc} and MPPT is seized. Grid synchronization and Q control is carried out by the GSC. | Not required (For longer dips pitch control may be required) | I_g and V_{dc} rises |
| [23] | AFER for V_{dc} regulation Active Sw.: 6 | AFER for MPPT, grid interface and I_g control Active Sw.: 6 | <ul style="list-style-type: none"> V_{dc} control is achieved by the MSC. MPPT is seized and no P is injected into the grid to keep the grid currents I_g within safe limit. Grid synchronization and Q control is carried out by GSC for grid support. Surplus energy is stored in rotor inertia. | Not required (Pitch control might be required if generator speed was critical) | I_g and V_{dc} rises |
| [21] | AFER for MPPT Active Sw.: 6 | AFER for V_{dc} control, grid interface and I_g control Active Sw.: 6 | <ul style="list-style-type: none"> V_{dc} control is achieved by the GSC. Grid interface and Q control is carried out by GSC according to; <ol style="list-style-type: none"> if $P_{gen} < P_{grid}$, generator power is set according to the maximum grid power capability with no Q support (MPPT is kept on). if $P_{gen} > P_{grid}$, crowbar action is activated with Q support and generator power is limited accordingly (MPPT is detained). MPPT alongside crowbar circuit is used if rotor speed is max. | Extra crowbar circuit is required | I_g and V_{dc} rises |
| [15] | AFER for V_{dc} control Active Sw.: 6 | AFER for MPPT, grid interface and I_g control Active Sw.: 6 | <ul style="list-style-type: none"> V_{dc} control is achieved by the MSC. MPPT is seized and no P is injected into the grid to keep the grid currents within safe limit. Grid synchronization and Q control done by GSC for grid support. Surplus energy is stored in rotor inertia. | Not required (Pitch control may be required for longer dips) | I_g and V_{dc} rises |
| [20] | AFER for MPPT Active Sw.: 6 | AFER for V_{dc} control, grid interface and I_g control Active Sw.: 6 | <ul style="list-style-type: none"> V_{dc} control is achieved by the MSC along with an ESS. MPPT is maintained as long as ESS has enough reserve to store active power surplus, otherwise MPPT is ended to keep I_g within safe limit. Grid synchronization and Q control is done by GSC for grid support. | ESS and its associated control are required | I_g and V_{dc} rises |
| [19] | AFER for MPPT Active Sw.: 6 | AFER for grid interface I_g control and V_{dc} regulation Active Sw.: 6 | <ul style="list-style-type: none"> MPPT is seized and V_{dc} control is achieved through a super capacitor energy storage element (SCES) operated according to dip severity. Grid synchronization and reactive power Q control is carried out by the GSC for grid support. Surplus energy is stored in rotor inertia in coordination with SCES. | Chopper controlled super—capacitor is required | I_g and V_{dc} rises |
| Proposed | Diode bridge rectifier + boost chopper for MPPT Active Sw.: 1 Passive Sw.: 7 | Three-phase VSI for V_{dc} control, grid interface and I_g control Active Sw.: 6 | <ul style="list-style-type: none"> MPPT is seized and V_{dc} control is done by MSC (De-coupled Action). P is injected into the grid is limited to keep the grid currents within safe limit in accordance to grid code. Grid synchronization and Q control is carried out by GSC. Surplus energy is stored in rotor inertia. | Not required (For longer severe dips pitch control may be required) | I_g and V_{dc} rises |

3. System under Consideration

As shown in Figure 2, the system under consideration is a PMSG-based WECS integrated to a three-phase grid via two conversion stages. An AC/DC conversion stage at the machine side applying a diode rectifier-boost topology followed by a DC/AC conversion stage at the grid side featuring a three-phase voltage source inverter (VSI).

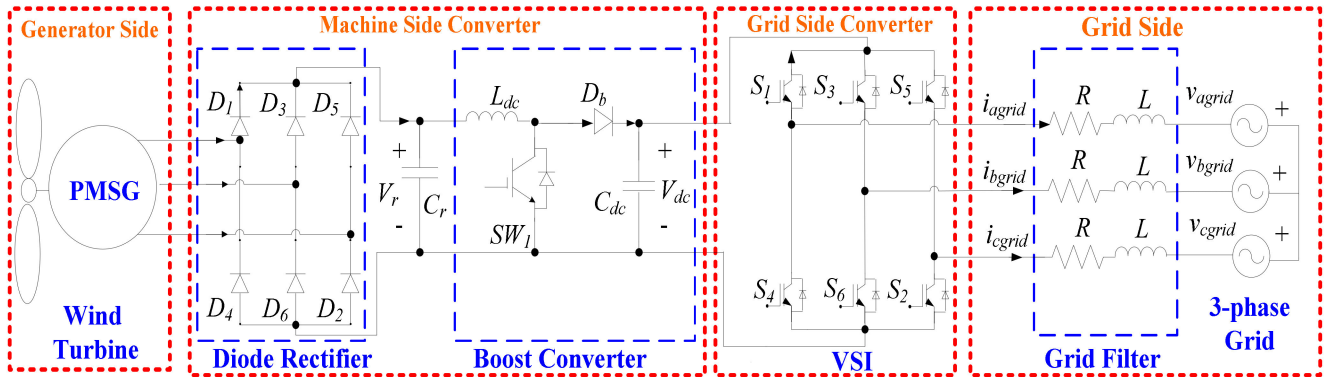


Figure 2. Schematic diagram of considered PMSG-based WECS.

3.1. Wind Turbine

Power captured by a wind turbine can be represented by (1) [36]:

$$P_w = \frac{1}{2} \rho A C_p(\lambda, \beta) V_w^3 \tag{1}$$

where ρ is the wind density, V_w is the wind speed, A is the wind turbine blade swept area and C_p is the turbine-rotor power coefficient that is a function of the tip speed ratio, λ , and the pitch blade angle β . The tip speed ratio λ is defined as the ratio between the blade tip speed ω , wind turbine blade radius r and the wind speed V_w and can be demonstrated by (2):

$$\lambda = \frac{r\omega}{V_w} \tag{2}$$

Thus, the mechanical power of the wind turbines can be controlled by λ and β . For every fixed β there is a corresponding $(C_p - \lambda)$ curve, where each has an optimum C_p (i.e., $C_{p_{opt}}$) value corresponding to an optimum λ (λ_{opt}). By controlling these values, the turbine mechanical power can be modulated to any power depending on the available wind speed. Maximum C_p is achieved at optimized rotational speed when β is equal to zero.

3.2. PMSG

The mechanical power from wind turbines is translated into electrical power using a PMSG. The PMSG voltage and current equations can be defined as in (3) and (4):

$$v_{dgen} = (R_a + pL_d)i_{dgen} - \omega_e L_q i_{qgen} \tag{3}$$

$$v_{qgen} = (R_a + pL_q)i_{qgen} + \omega_e L_d i_{dgen} + \varphi_f \omega_e \tag{4}$$

where v_{dgen} and v_{qgen} are the PMSG stator dq axis voltages, and i_{dgen} and i_{qgen} represent the PMSG stator currents, respectively. L_d , L_q and R_a indicate the stator dq axis inductances and resistance, respectively. ω_e is the electrical angular frequency.

The electromechanical developed torque T_e is obtained as given by (5):

$$T_e = \frac{3}{2} \left(\frac{p}{2} \right) \left(\varphi_f i_{qgen} + (L_d - L_q) i_{qgen} i_{dgen} \right) \tag{5}$$

where φ_f is the amplitude permanent magnet flux linkage and p is the number of pole pairs.

The torque and mechanical speed can be related using (6), where J is the moment of inertia, ω_r is the rotor mechanical angular frequency and T_L is the load torque.

$$T_e = J \left(\frac{2}{P} \right) \frac{d\omega_r}{dt} + \omega_r \left(\frac{2}{P} \right) + T_L \tag{6}$$

3.3. MSC

Since the generator output voltage and frequency do not match those of the grid, the AC/DC conversion unit at the machine side, transforms generator output voltage and current to DC values, thus becoming frequency independent. This conversion stage features a three-phase diode rectifier that converts generator output voltage to a DC voltage, followed by a boost chopper which normally achieves MPPT.

The mean value of the rectifier output voltage \bar{V}_r is given by (7):

$$\bar{V}_r = \frac{1}{\frac{\pi}{3}} \int_{\frac{\pi}{6}}^{\frac{\pi}{2}} \sqrt{2} V_{LL} \sin \left(\omega_s t + \frac{\pi}{6} \right) d(\omega_s t) = \frac{3\sqrt{2}}{\pi} V_{LL} \approx 1.35 V_{LL} \tag{7}$$

where V_{LL} is the rms value of the line-to-line input voltage and ω_s is the input voltage angular frequency.

The rectified voltage V_r is boosted to the DC-link voltage (V_{dc}) via the boost converter of transfer function given by (8) assuming continuous inductor current.

$$\frac{V_{dc}}{V_r} = \frac{1}{1-d} \tag{8}$$

where d is the duty cycle, defined as (9):

$$d = \frac{t_{on}}{T} \tag{9}$$

where t_{on} is the switch ON time, T is the switching period and t_{off} is the switch OFF time.

The inductor ripple current Δi_b of the boost converter can be expressed by (10), while the converter peak-to-peak output voltage ripple Δv_{dc} is given by (11):

$$\Delta i_b = d (1-d) \frac{V_{dc} T}{L_{dc}} \tag{10}$$

$$\Delta v_{dc} = \frac{d T V_{dc}}{R_{Load} C_{dc}} \tag{11}$$

where L_{dc} , C_{dc} and R_{Load} are the boost chopper inductor, output capacitor and equivalent load resistance, respectively.

3.4. GSC

For successful WECS—grid interface in accordance with grid regulations and standards—a DC/AC conversion stage is applied at the grid side. A sinusoidal pulse-width-modulated (SPWM) current-controlled three-phase VSI is adopted in this stage owing to its low cost, ease of control and stable open-loop operation using constant V/Hz control. The maximum amplitude of the line-to-line inverter output voltage, $(\hat{V}_{LLinv})_{max}$, in the SPWM is limited to (12):

$$(\hat{V}_{LLinv})_{max} = \frac{\sqrt{3}}{2} V_{dc} \approx 0.867 V_{dc} \tag{12}$$

3.5. Grid Side Filter

A first-order *RL* filter is applied for grid current smoothing; otherwise, current distortions, if injected into the grid, can cause the malfunction of sensitive apparatus connected to the same bus. Hence, the grid voltage per phase is given by (13):

$$v_{grid} = Ri_{grid} + L \frac{di_{grid}}{dt} + V_{PCC} \tag{13}$$

where v_{grid} , i_{grid} are the grid voltage and injected grid current, respectively, R , L are the equivalent resistance and inductance of distribution lines and applied passive filter, respectively, and V_{PCC} is the voltage at the PCC.

3.6. Inverter DC-LINK

The inverter DC-link offers a buffering stage between the MSC and the GSC, where the energy balance equation can be represented by (14):

$$P_{gen} = C_{dc} \frac{dV_{dc}}{dt} + i_{grid}^2 R + P_{grid} \tag{14}$$

where P_{gen} and P_{grid} represent the PMSG generator extracted power and grid injected power, respectively. It should be noted that in case of normal operation, both P_{gen} and P_{grid} are equal ignoring converters and grid losses. This should be guaranteed to maintain energy balance at this link and in turn the DC-link voltage is regulated and system robustness is maintained. Thus, this DC-link is considered the system core and the dynamic model at this zone is derived to verify the proposed system stability as follows:

State-space models give a basic and powerful method for the dynamic modelling of numerous systems (continuous and discrete, linear and non-linear, time-variant and invariant systems). Thus, they are mostly convenient to model the steady-state and the dynamic performances of the power electronic converters. The method of State-Space Averaging was developed to characterize the transfer properties of switching converter power stages. This method has been very well received by the power electronics industry, in contrast to other approaches, which give little or no insight into the design and behavior of the converter [37,38].

In the considered work, the boost converter output DC-link capacitor is also placed at the input of the three-phase VSI. Hence, it is not only affected by the rippled DC waveforms of the boost converter, but also by the VSI AC waveforms. Therefore, state space is the best modeling technique to model the considered time-invariant non-linear system [39,40].

It is worth noting that the VSI output signals are AC waveforms while the VSI input signals as well as those of the boost converter are DC waveforms associated with AC component oscillating around the average value as shown in (15):

$$x = X + \hat{x} \tag{15}$$

The VSI input and output signals are related as follows:

$$v_{inv} = \frac{m}{2} v_{dc} \tag{16}$$

where the modulation index $m = M \sin(2\pi 50t + \theta)$, v_{inv} is the VSI output AC voltage, while v_{dc} is the VSI input rippled DC voltage. For lossless VSI,

$$v_{dc} i_{dc} = v_{inv} i_{grid} \tag{17}$$

$$i_{dc} = \frac{m}{2} i_{grid} \tag{18}$$

where i_{grid} is the VSI output AC sinusoidal current, while i_{dc} is the VSI input rippled DC current.

The dynamic model of the considered system topology, at the DC-link, is derived using State-Space Averaging. Switching periods of the boost chopper is described by two circuit topologies (continuous conduction mode), i.e., two sub-models each addressing system-specific circuit dynamics as shown in Figure 3. The first sub-model offers the state-space dynamic equation of the system when the boost converter switch (SW1) is at the ON state as shown in Figure 3a. On the other hand, the second sub-model shows the dynamic model when the switch (SW1) is OFF, as demonstrated by Figure 3b. For the sake of simplicity, capacitors and inductors’ internal resistances are neglected while the diode is modeled as a short circuit in ON-state and open circuit in OFF-state.

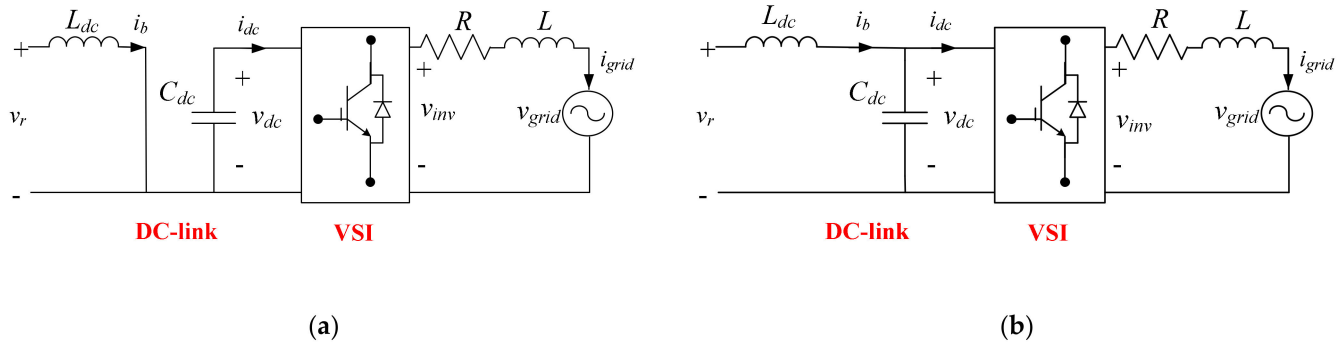


Figure 3. System’s sub-model circuits when SW1 is (a) ON and (b) OFF.

- When SW1 is ON, applying Kirchoff’s voltage and current laws, the following results are found:

$$L_{dc} \frac{d i_b}{dt} = v_r \tag{19}$$

$$C_{dc} \frac{d v_{dc}}{dt} = -\frac{m}{2} i_{grid} \tag{20}$$

$$L \frac{d i_{grid}}{dt} = \frac{m}{2} v_{dc} - i_{grid} R - v_{grid} \tag{21}$$

where i_b, v_r, v_{dc} are the instantaneous boost converter current, rectifier output voltage and DC-link voltage, respectively.

Equations (19)–(21) are rearranged to obtain the state-space sub-model shown in (22):

$$\begin{bmatrix} \dot{i}_b \\ \dot{v}_{dc} \\ \dot{i}_{grid} \end{bmatrix} = A_1 \begin{bmatrix} i_b \\ v_{dc} \\ i_{grid} \end{bmatrix} + B_1 \begin{bmatrix} v_r \\ v_{grid} \end{bmatrix} \tag{22}$$

where

$$A_1 = \begin{bmatrix} 0 & 0 & 0 \\ 0 & 0 & -\frac{m}{2C_{dc}} \\ 0 & \frac{m}{2L} & -\frac{R}{L} \end{bmatrix} \text{ and } B_1 = \begin{bmatrix} \frac{1}{L_{dc}} & 0 \\ 0 & 0 \\ 0 & -\frac{1}{L} \end{bmatrix} \tag{23}$$

- When SW1 is OFF applying Kirchoff’s voltage and current laws, the following results are found:

$$L_{dc} \frac{d i_b}{dt} = v_r - v_{dc} \tag{24}$$

$$C_{dc} \frac{d v_{dc}}{dt} = i_b - \frac{m}{2} i_{grid} \tag{25}$$

$$L \frac{d i_{grid}}{dt} = \frac{m}{2} v_{dc} - i_{grid} R - v_{grid} \tag{26}$$

Equations (24)–(26) are rearranged to obtain the state-space sub-model shown in (26):

$$\begin{bmatrix} \dot{i}_b \\ \dot{v}_{dc} \\ \dot{i}_{grid} \end{bmatrix} = A_2 \begin{bmatrix} i_b \\ v_{dc} \\ i_{grid} \end{bmatrix} + B_2 \begin{bmatrix} v_r \\ v_{grid} \end{bmatrix} \tag{27}$$

where

$$A_2 = \begin{bmatrix} 0 & -\frac{1}{L_{dc}} & 0 \\ \frac{1}{C_{dc}} & 0 & -\frac{m}{2C_{dc}} \\ 0 & \frac{m}{2L} & -\frac{R}{L} \end{bmatrix} \text{ and } B_2 = \begin{bmatrix} \frac{1}{L_{dc}} & 0 \\ 0 & 0 \\ 0 & -\frac{1}{L} \end{bmatrix} \tag{28}$$

The state-space averaging approach offers clear insight into the entire system dynamics, where:

$$\left. \begin{aligned} \bar{A} &= A_1 * d + A_2 * (1 - d) \\ \bar{B} &= B_1 * d + B_2 * (1 - d) \end{aligned} \right\} \tag{29}$$

where d is the boost converter duty ratio.

Hence, applying the latter to system state space sub-models, presented in (22) and (27), the total averaged state-space model of the considered system is given by (30):

$$\begin{bmatrix} \dot{i}_b \\ \dot{v}_{dc} \\ \dot{i}_{grid} \end{bmatrix} = \bar{A} \begin{bmatrix} i_b \\ v_{dc} \\ i_{grid} \end{bmatrix} + \bar{B} \begin{bmatrix} v_r \\ v_{grid} \end{bmatrix} \tag{30}$$

where

$$\bar{A} = \begin{bmatrix} 0 & -\frac{(1-d)}{L_{dc}} & 0 \\ \frac{(1-d)}{C_{dc}} & 0 & -\frac{m}{2C_{dc}} \\ 0 & \frac{m}{2L} & -\frac{R}{L} \end{bmatrix} \text{ and } \bar{B} = \begin{bmatrix} \frac{1}{L_{dc}} & 0 \\ 0 & 0 \\ 0 & -\frac{1}{L} \end{bmatrix} \tag{31}$$

From matrix \bar{A} , proposed system stability constraints can be determined. First, get the model characteristic equation by setting the following:

$$|\lambda I - \bar{A}| = 0 \tag{32}$$

where λ is the model eigenvalues, while I is an identity matrix of dimension 3×3 . Then, Routh’s stability criterion is applied. From the latter, it can be deduced that for the proposed model to be stable, both criteria, demonstrated in (33) and (34), should be fulfilled:

$$\frac{(1-d)^2 R}{LL_{dc}C_{dc}} > 0 \tag{33}$$

$$\frac{M^2 R}{8L^2 C_{dc}} + \frac{(1-d)^2 R}{LL_{dc}C_{dc}} > \frac{(1-d)^2 R}{LL_{dc}C_{dc}} \tag{34}$$

4. Proposed LVRT Control Scheme

For successful grid interface, the WECS must satisfy the grid requirements during normal and low voltage conditions [41–43]. In this paper, a control scheme is proposed, enabling the MSC and GSC controllers to fulfill the following control goals during MPPT and non-MPPT (LVRT) operation modes shown in Figure 4, where V_d is the grid voltage d -axis component.

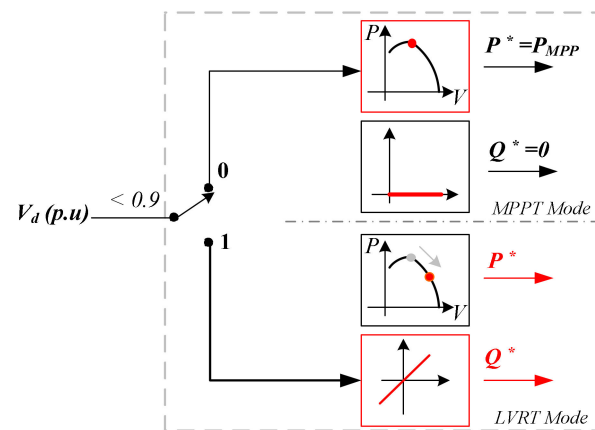


Figure 4. Operation modes of system under consideration.

MPPT mode (during normal grid conditions):

- MPPT for maximum wind energy harvesting.
- DC-link voltage regulation.
- Grid synchronization and active power injection into utility.
- Grid current control to ensure high quality and unity power factor.

LVRT mode (during voltage sag conditions):

- MPPT is seized and output active power is limited to eliminate grid current rises to avoid the tripping of the inverter overcurrent protection [31].
- DC-link voltage regulation.
- Grid synchronization and reactive power injection into the grid, according to grid regulations, to support grid voltage during recovery.
- Grid current high quality is preserved during LV conditions.
- Any mismatch, between generator and grid powers, is stored in rotor inertia.

4.1. Converters' Controllers

In the considered grid-tied wind energy system, there are two main current controlled converters, which are the diode rectifier-boost converter at the machine side and the three-phase voltage source inverter at the grid side. Four control variables need to be tightly controlled, which are the generator active power, the DC-link voltage and grid active and reactive powers. This is done by the MSC and GSC controllers as shown in Figure 5.

- The rectified voltage produced by the diode rectifier V_r varies with generator speed. However, the DC-link voltage must be regulated at a constant value in order to maintain energy balance at the DC-link; thus, active power transfer to grid is guaranteed. DC-link voltage control is carried out by GSC during MPPT mode, then it is swapped to the MSC during LVRT mode, as will be discussed later.
- Generator power is controlled via the MSC PI controller, which forces the boost chopper current I_b to follow a command value I_b^* . This reference signal depends on system operating mode, i.e., at MPPT mode it is determined to satisfy maximum power extraction from the wind turbine, whereas during low voltage it is chosen to extract the active power adequate to just regulate the DC-link voltage.
- Grid synchronization during different operation modes is achieved via the GSC PI controllers, which control the active and reactive powers injected into the grid by controlling the grid current d and q components. This control strategy is the dq synchronous reference frame control, which uses a reference frame transformation, from $abc \rightarrow dq$ to transform the grid current and voltage waveforms into a reference frame that rotates synchronously with the grid voltage using the Park's and Clark's transformations. Transforming the AC quantities into DC values leads to easier filtering and control. However, these transformations require the instantaneous grid

voltage phase-angle θ_u , which is detected by synchronizing the PLL rotating reference frame to the utility-voltage vector [44].

4.2. Currents' Reference Generation

As discussed earlier, to control the generator power, the MSC controller forces the boost current to follow a certain set point, whereas the GSC controllers force the grid current dq components to follow certain references for grid interface. In the proposed control scheme, currents' references vary according to operation mode to guarantee safe and efficient operation of wind turbines and meanwhile meet the grid codes. The proposed currents' reference generation scheme is presented in Figure 6 and is explained in each mode as follows:

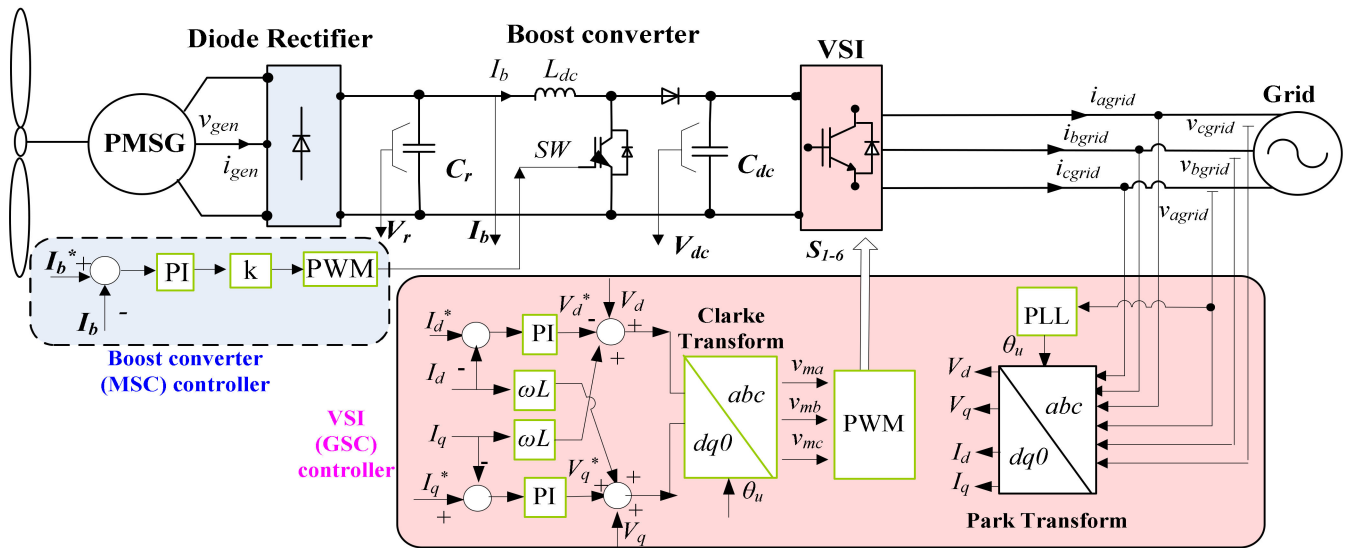


Figure 5. MSC and GSC controllers for the considered PMSG WECS.

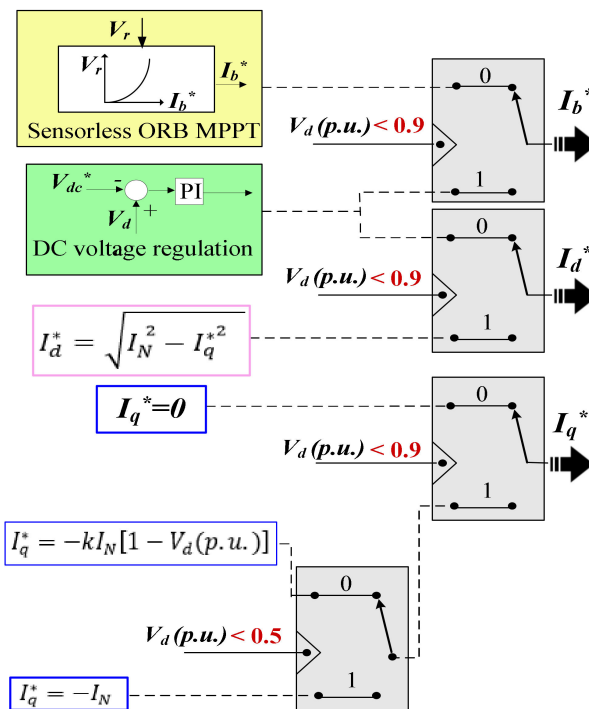


Figure 6. Reference generation for system converters' controllers during normal operation and grid voltage dips.

4.2.1. During MPPT Mode

For the optimal operation of variable speed wind turbine power systems, MPPT is mandatory. Hereby, the optimum relationship-based (ORB) sensorless MPPT approach is applied [45–47]. In this method, instead of relying on mechanical sensors to measure wind and generator speeds, parameters are calculated from available electrical parameters at the generator output terminals. For every wind speed, there is a peak power P_{MPP} , which corresponds to an optimal DC power at rectifier output P_{r-opt} , i.e., corresponding to an optimal rectified voltage value V_{r-opt} and current I_{r-opt} , as shown in (35):

$$P_{r-opt} = \eta P_{MPP} = V_{r-opt} I_{r-opt} \tag{35}$$

where η is the conversion efficiency from the generator to the rectifier DC-side and is assumed to be a fixed value.

The rectified current in the considered system is the boost converter current I_b . Thus, using the sensorless ORB technique, the optimum relationship between the rectifier output voltage V_r and boost chopper current I_b is recorded in a lookup table for different wind speeds. In the MPPT mode, the boost current reference is determined according to the ORB sensorless approach to guarantee maximum wind power extraction. On the other hand, the GSC should guarantee DC-link voltage regulation, grid synchronization and grid current control to achieve a high level of quality and unity power factor. Thus, the reference of grid current d component I_d^* is determined via the DC-link voltage regulation loop, while the grid current q component reference I_q^* is set to zero to allow only the harvested active power to be injected into the grid.

4.2.2. During LVRT Mode

In this mode, the MPPT is seized to limit rises in grid current and the boost chopper overtakes DC-link voltage regulation. Thus, the reference for the boost converter current I_b^* is produced from the DC-link voltage regulation loop. On the other hand, according to grid regulations, reactive power should be injected during sag conditions. The amount of reactive power that should be injected is dependent on the voltage sag depth and the inverter rated current, noting zero reactive grid current before the voltage dip. Thus, the reference for the grid current q -axis I_q^* component varies, as shown in (36), in accordance with Eon-Netz grid codes [25,48].

$$I_q^* = \begin{cases} 0 & 0.9 \leq V_d(p.u.) < 1.1 \\ -kI_N[1 - V_d(p.u.)] & 0.5 \leq V_d(p.u.) < 0.9 \\ -I_N & V_d(p.u.) < 0.5 \end{cases} \tag{36}$$

where k is a constant given by (37):

$$k = \frac{\Delta I_q(p.u.)}{\Delta V_d(p.u.)} \geq 2 \tag{37}$$

where I_N is the nominal grid current limited by the inverter maximum rating current, ΔI_q is the change in grid current q -axis component and ΔV_d is the change in grid voltage d -axis component. Thus, based on voltage sag depth, I_q^* is determined and, accordingly, the reference for the grid current d -axis component I_d^* is calculated from (38).

$$I_d^* = \sqrt{I_N^2 - I_q^{*2}} \tag{38}$$

It is clear that the proposed scheme features grid current control decoupled from the DC-link voltage control during LV conditions. This can be concluded from Figure 6, where I_d^* and I_q^* are computed independently of V_{dc} loop. This improves the robustness of the applied control system during faults and prevents the transfer of noise and power ripples at the DC-link into the grid, thus preserving the grid current’s high quality.

5. Simulation Results

A PMSG-based WEC grid-tied system is considered in simulation work for validating the proposed approach. Simulated system-rated parameters are listed in Table 2, where the wind turbine is driven at a fixed wind speed of 12 m/s and constant blade pitch angle $\beta = 0$. The turbine drives a 1.5 MVA, 80 poles, 11.5 Hz, gearless PMSG at $690\sqrt{3}$ V line-to-line generator voltage, and fixed rated speed ω_r of 1.8 rad/s. The diode rectifier converts the generator voltage to a DC voltage, which is then boosted by the boost chopper of 5 kHz switching frequency. During normal operation, the boost chopper controller guarantees MPPT, whereas the three-phase VSI, operating at 5 kHz carrier frequency, is responsible for DC-link voltage regulation to 5500 V and WECS integration to a 480 V, 50 Hz utility grid at unity power factor and 4% THD. For wind speed of 12 m/s, the tracked power, which is injected into the grid during normal conditions, reaches almost 765 kW.

Table 2. Rated parameters of the WECS considered for simulation.

| Variable | Parameter | Value |
|-------------|--|--------------------|
| P_w | Turbine rated Power (MW) | 1.5 |
| V_w | Rated wind speed (m/s) | 13 |
| R | Turbine rotor diameter (m) | 54.4 |
| A | Swept area (m^3) | 2324.27 |
| n | Number of blades | 3 |
| P_{gen} | Generator rated power (MW) | 1.5 |
| f_{gen} | Generator frequency (Hz) | 11.5 |
| P | Pole pairs of PMSG | 40 |
| v_{gen} | Generator phase voltage | 690 |
| Hz | Frequency | 11.5 |
| ω_r | Mechanical angular frequency (rad/s) | 1.8 |
| J | Generator Inertia constant ($M\ kg.m^2$) | 0.92 |
| T_e | Generator torque (M N.m) | 0.83 |
| φ_f | Permanent magnet flux linkage (V/rad/s) | 8 |
| L_d | d-axis inductance (mH) | 4×10^{-3} |
| L_q | q-axis inductance (mH) | 4×10^{-3} |
| R_a | Stator resistance (Ω) | 0.000317 |
| C_r | Rectifier output capacitor (μF) | 5000 |
| f_c | Boost chopper and VSI switching frequency (Hz) | 5000 |
| L_{dc} | Boost chopper inductor (mH) | 10 |
| C_{dc} | DC-link capacitor (μF) | 6000 |
| V_{dc} | DC-link voltage (V) | 5500 |
| v_{grid} | Grid voltage (V) | 480 |
| f_{grid} | Grid frequency (Hz) | 50 |
| R | Grid filter resistance (Ω) | 0.02 |
| L | Grid filter inductance (mH) | 10 |

The system has been simulated using MATLAB/Simulink during two voltage sag cases: 30% and 70% grid voltage dips. For comparison, the WECS was simulated once without the proposed technique, then when applying the swap proposed control methodology. Table 3 briefs simulation results during both dip cases.

5.1. Case 1: 70% Symmetrical Grid Voltage Dip

System performance has been investigated for a 70% three-phase symmetrical voltage sag occurring at the PCC at $t = 0.6$ and was cleared at $t = 0.75$ s (i.e., sag duration is 150 ms), and the results are demonstrated in Figure 7.

Table 3. Simulation performance results.

| Results during Fault | During 70% Voltage Sag | | During 30% Voltage Sag | |
|----------------------|------------------------|-------------------------|------------------------|-------------------------|
| | No Mode-Shift Control | With Mode-Shift Control | No Mode-Shift Control | With Mode-Shift Control |
| I_b (A) | 1 | 0 | 1 | 0.6 |
| I_d (A) | 1.2 | 0 | 1.1 | 0.6 |
| I_q (A) | 0 | −1 | 0 | −0.8 |
| $I_{grid, peak}$ (A) | 1.2 | 1 | 1.1 | 1 |
| %THD | 6% | 3% | 5.5% | 4% |
| V_{dc} (V) | 1.2 | 1.05 | 1.1 | 1.02 |
| P_{grid} (W) | 0.336 | 0 | 0.77 | 0.325 |
| Q_{grid} (W) | 0 | 0.28 | 0 | 0.45 |

During the dip incident, the MSC continues to extract maximum power from wind, while the GSC achieves DC-link voltage regulation and grid synchronization at unity power factor. Due to the drop in grid voltage v_{grid} to 0.3 p.u., the grid currents i_{grid} will rise accordingly to almost 1.2 of its rated value, while the active power injected into the grid P_{grid} is reduced significantly. At the generator side, the MSC does not sense or detect the sag incident; thus, the boost chopper current I_b will continue to track the chopper reference current I_b^* corresponding to the MPPT operation. MSC control is unaltered; therefore, no observed changes are indicated in the generator speed, torque, output line voltage v_{ab-gen} , or its line current i_{a-gen} , meaning the generator maximum power P_{gen} is still extracted. Due to the energy imbalance, the PMSG will inject its active power into the DC-link, causing a rise in the DC-link voltage V_{dc} that exceeds its rated value by almost 20%. In response to the DC-link voltage rise, the GSC d -axis current I_d^* controller command rises, to maintain the energy balance and deliver all the energy stored in the DC-link capacitor to the grid, thus hitting the grid current limitations. Meanwhile, grid reactive power Q_{grid} is maintained to zero due to unity power factor operation; thus, the q -axis current I_q^* controller command remains at zero. In real systems, grid current rise can hit the converter thermal limits, and this may destroy the power converters due to voltage and current stresses on the power modules. As the fault is cleared at $t = 0.75$ s, grid voltage v_{grid} recovers to 1p.u. DC-link voltage V_{dc} takes time for recovery as it is governed by the dynamics of the DC-link voltage control loop and the DC-link capacitor C_{dc} value. Grid currents and power return to pre-fault values and the system fully recovers at $t = 1.45$ s.

To validate the proposed approach's effectiveness, the system is retested when swapping the control during the dip duration. Figure 8 shows the system response after applying the proposed control methodology for a similar 70% symmetrical voltage sag. During the sag, the MSC and GSC will switch actions as previously explained, where the MPPT is seized and the MSC takes charge of DC-link voltage regulation, which is achieved decoupled from the grid current control achieved by the GSC. This decoupled action prevents DC-link voltage ripple propagation to the grid, reducing grid current THD during the dip from 6% (when applying non swap control) to 3% (with the proposed swap control). The GSC takes control of the grid interface and supports by injecting reactive power into the grid while limiting active power injection. Thus, DC-link voltage rise and grid currents' increases are eliminated. According to the voltage dip depth, the GSC will operate to provide full reactive power support with no active power exported to the grid. In order to achieve the latter, the grid q -axis current reference I_q^* is adjusted to $-I_N$ in accordance with Equation (36), while the d -axis current command I_d^* is set to zero; thus, grid current increase is eliminated. The DC-link voltage V_{dc} is now being regulated solely by the MSC to its rated value. Meanwhile, MPPT is halted, so the boost converter current I_b will drop to zero, allowing the energy surplus to be stored in the generator's rotating mass. Accordingly, PMSG line current i_{a-gen} and PMSG active power P_{gen} are reduced to zero in response to the MPPT termination. Consequently, there is a torque mismatch in the mechanical system turbine-generator, which causes the PMSG rotor speed n to increase due to the reduction

in the electromagnetic torque T_e [27]. However, due to the large inertia of the mechanical wind turbine system, speed increase is maintained within the safety operating margins of the generator and does not exceed 130%.

After the dip is cleared, both converters switch back to their normal control actions prior to the fault. The MSC achieves MPPT, controls the PMSG active power and maintains the generator speed. Speed n is recovered as well as the electromagnetic torque T_e , and the energy stored in the inertia is transferred smoothly to the grid. DC-link voltage regulation, as well as grid synchronization at unity power factor, is restored by GSC, and the system recovers at $t = 1.1$ s.

5.2. Case 2: 30% Symmetrical Grid Voltage Dip

The system performance has been assessed for a three-phase symmetrical dip of 30% at the PCC occurring at $t = 0.6$ s for 150 msec. Similar to the 70% case, the system response was analyzed first with the conventional non-swap control methodology as shown in Figure 9, where the MSC continues to extract maximum power during the dip interval. The grid voltage v_{grid} drops to 0.7 p.u., while the grid current i_{grid} will increase above the nominal value. The GSC is unable to maintain the DC-link voltage V_{dc} regulated level due to the energy mismatch between the grid active power P_{grid} , which has been significantly reduced, and the extracted generator power P_{gen} . No reactive power support is provided during the fault; thus, the grid reactive power Q_{grid} is maintained at zero.

Figure 10 shows the system responses when the proposed control is applied during the same three-phase 30% symmetrical voltage dip. At $t = 0.6$ s, grid sag is detected, MPPT is seized, and power converters control duties are swapped. The MSC will take control of the DC-link voltage regulation while the GSC will control reactive and active power injection into the grid. According to the proposed control scheme, since the grid voltage v_{grid} falls between 0.5 and 0.9 p.u., reactive power support is required, and active power is set, accordingly, to prevent grid over currents.

This is achieved by setting the q -axis current I_q^* controller command using (36) the d -axis current command I_d^* , which is set as to $\sqrt{I_N^2 - I_q^{*2}}$ to keep the grid currents i_{grid} at nominal value. Grid current THD during the dip decreased to 4% due to the proposed decoupled control. Meanwhile, the DC-link voltage V_{dc} is maintained by the MSC within safe limits for safe ride-through and limiting the rise compared to the conventional control technique. After the fault is cleared at $t = 0.75$ s, GSC and MSC actions are restored, MPPT by MSC, while GSC injects the extracted power into the grid and maintains fixed DC-link voltage. Speed and torque are retained, and the system fully returns to normal operation at $t = 1.1$ s.

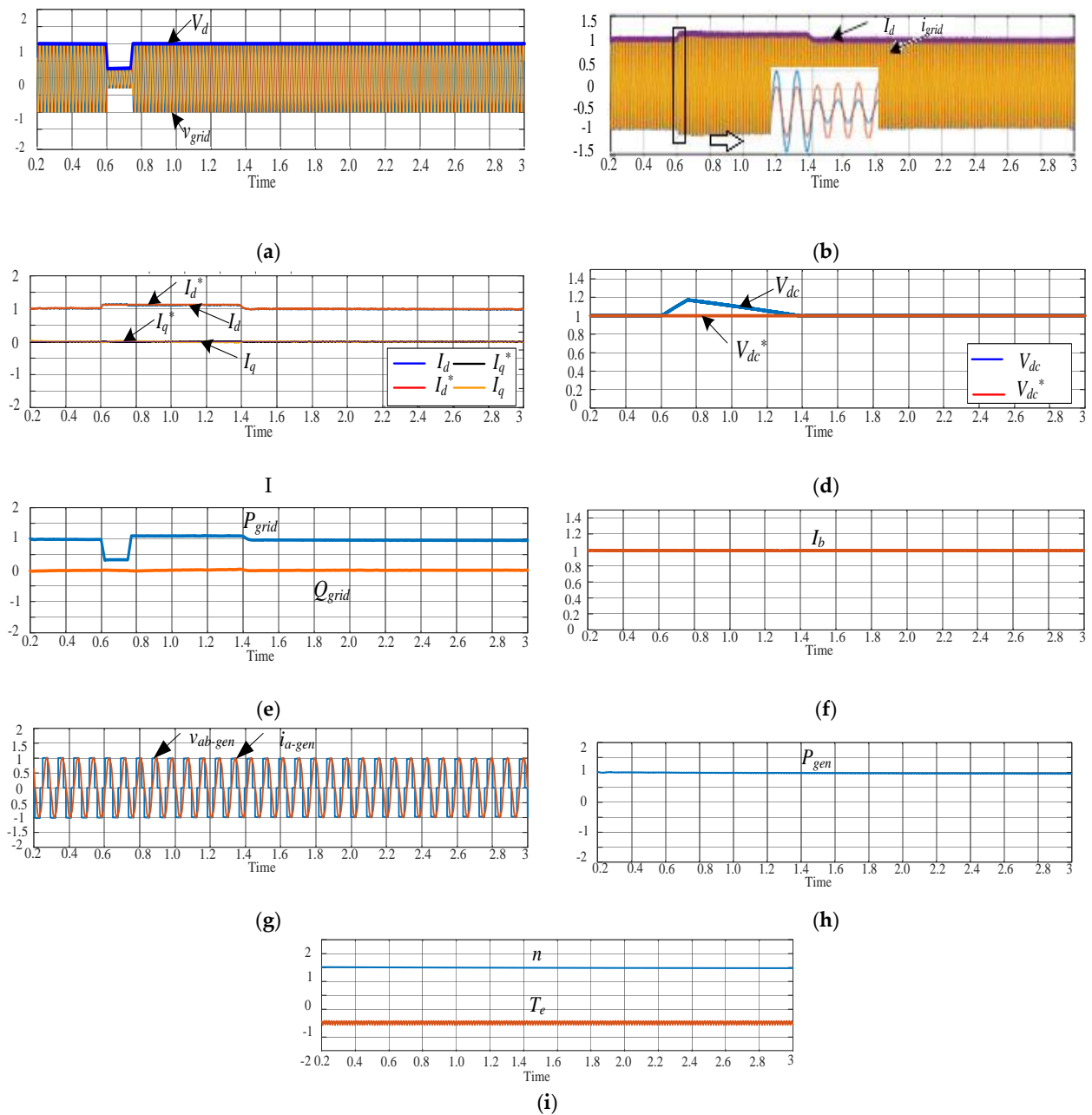


Figure 7. Simulation results during 70% symmetrical grid voltage without the proposed control scheme: (a) abc grid voltages v_{grid} and d– axis grid voltage V_d (p.u.); (b) abc grid currents i_{grid} and d– axis grid current I_d (p.u.); (c) d– axis currents I_d and reference I_d^* with q– axis currents I_q and reference I_q^* ; (d) DC– link voltage V_{dc} and reference V_{dc}^* (p.u.); (e) grid active power P_{grid} and reactive power Q_{grid} (p.u.); (f) boost chopper current I_b and reference I_b^* (p.u.); (g) PMSG Line–line voltage v_{ab-gen} and phase a– current i_{a-gen} ; (h) PMSG active power P_{gen} (p.u.); (i) PMSG speed n and torque T_e (p.u.).

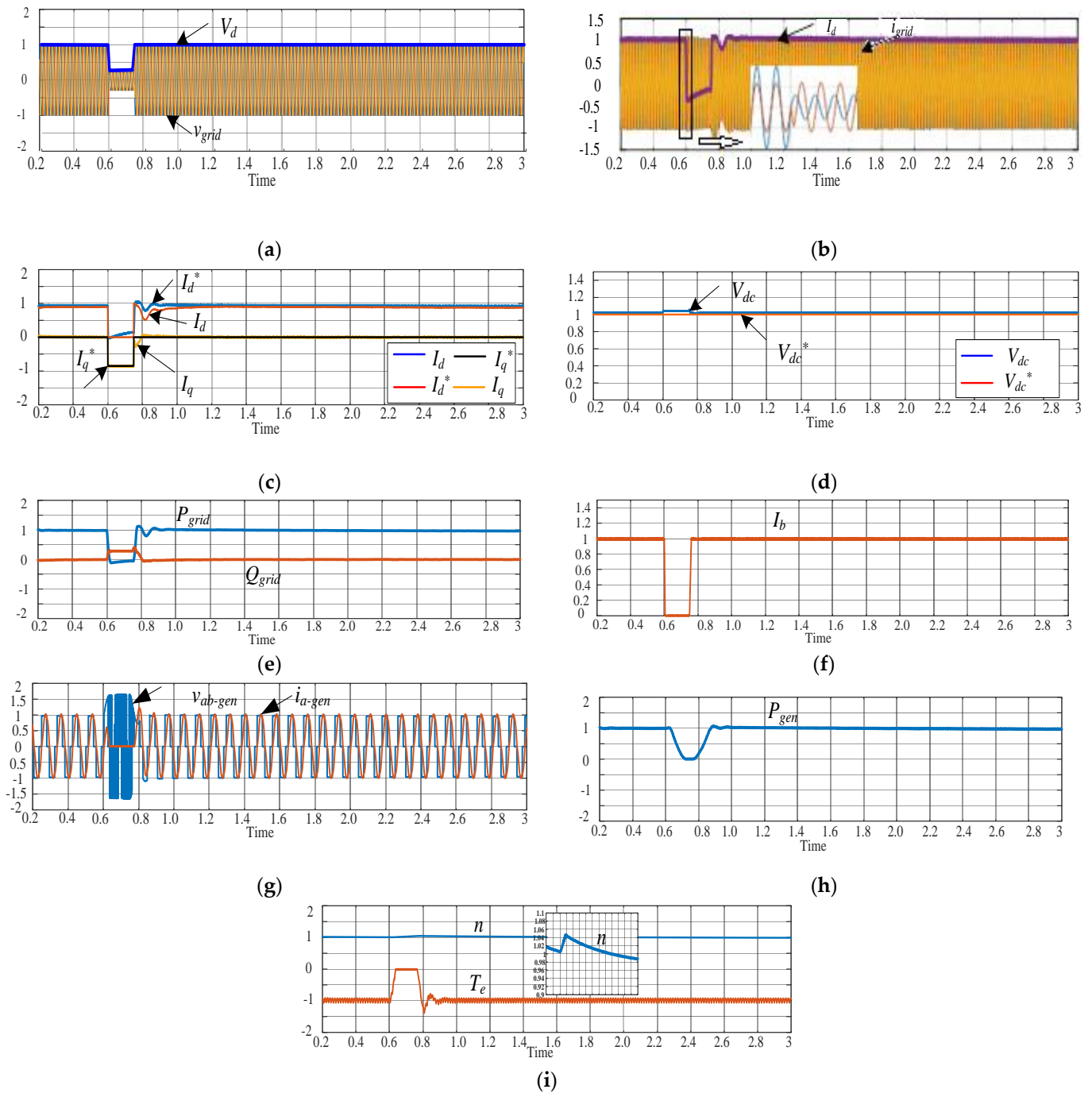


Figure 8. Simulation results during 70% symmetrical grid voltage dip with the proposed control scheme: (a) abc grid voltages v_{grid} and d-axis grid voltage V_d (p.u.); (b) abc grid currents i_{grid} and d-axis grid current I_d (p.u.); (c) d-axis currents I_d and reference I_d^* with q-axis currents I_q and reference I_q^* ; (d) DC-link voltage V_{dc} and reference V_{dc}^* (p.u.); (e) grid active power P_{grid} and reactive power Q_{grid} (p.u.); (f) boost chopper current I_b and reference I_b^* (p.u) (g) PMSG Line-line voltage v_{ab-gen} and phase a-current i_{a-gen} ; (h) PMSG active power P_{gen} (p.u); (i) PMSG speed n and torque T_e (p.u).

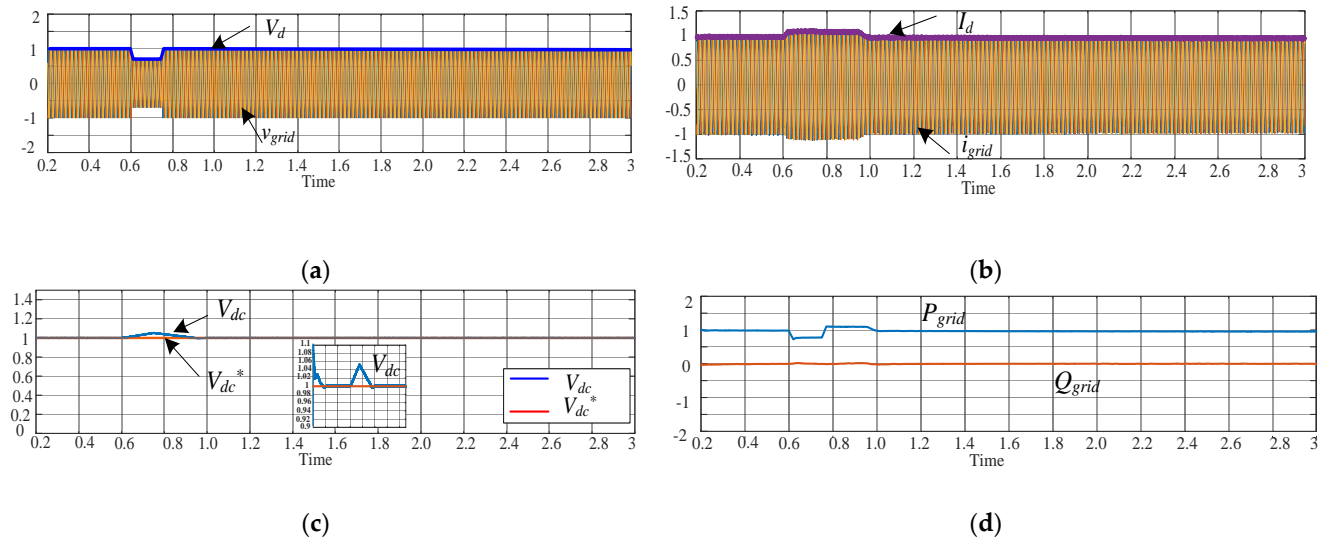


Figure 9. Simulation results during 30% symmetrical grid voltage dip without the proposed control scheme: (a) abc grid voltages v_{grid} and d– axis grid voltage V_d (p.u.); (b) abc grid currents i_{grid} and d– axis grid current I_d (p.u.); (c) DC– link voltage V_{dc} and reference V_{dc}^* (p.u.); (d) grid active power P_{grid} and reactive power Q_{grid} (p.u.).

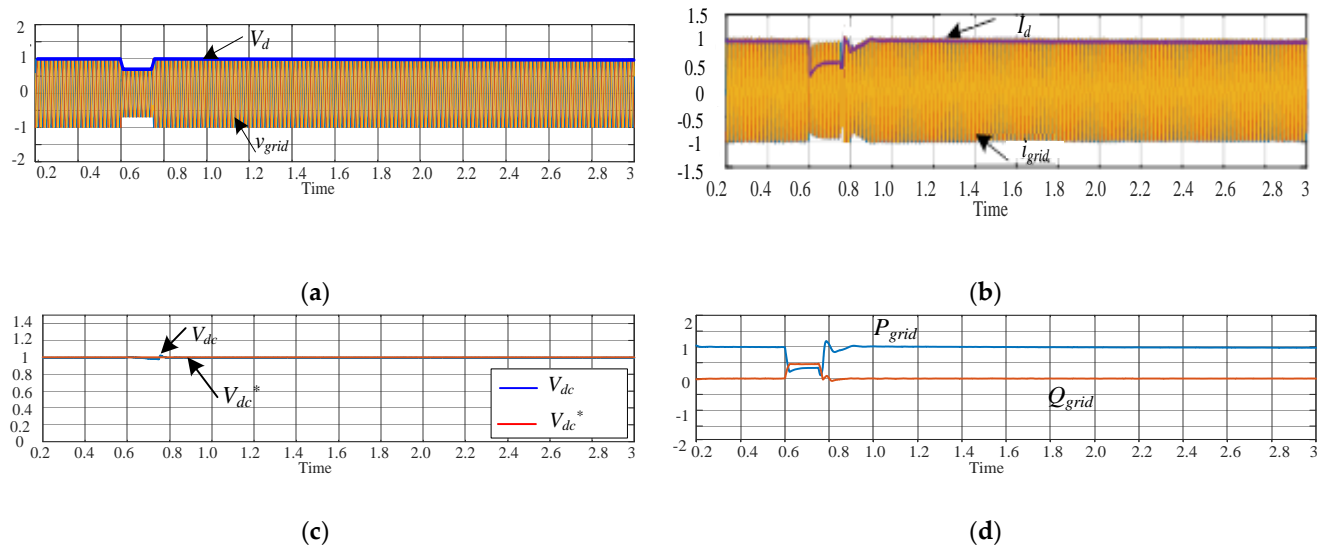


Figure 10. Simulation results during 30% symmetrical grid voltage with the proposed control scheme: (a) abc grid voltages v_{grid} and d– axis grid voltage V_d (p.u.); (b) abc grid currents i_{grid} and d– axis grid current I_d (p.u.); (c) DC– link voltage V_{dc} and reference V_{dc}^* (p.u.); (d) grid active power P_{grid} and reactive power Q_{grid} (p.u.).

6. Experimental Verification

Practical validation of the proposed approach has been applied to a low-power prototype of schematic diagram presented in Figure 11 and the rig photograph shown in Figure 12. The experimental rig parameters are listed in Table 4. Two mechanically coupled machines are employed (a DC-motor and a PMSG) to emulate the PMSG-wind turbine system. The experimental results are obtained when the PMSG is driven at a constant speed n of 900 rpm and produces a balanced 3-phase output voltage v_{gen} at a frequency f_{gen} of 30 Hz. The difference between the prototype PMSG and the simulated system frequency is the reduced number of poles available in the experimental prototype. Assuming that the MPPT algorithm for the wind turbine is at a steady state (fixed wind speed), the system is tested at a constant driven rotor speed instead of using a mechanical wind turbine.

Correspondingly, the boost converter current I_b is set to 2A and the generator extracted power P_{gen} is 100 W. To ensure a safe test rig operation, a 100 V V_{dc} has been selected since DC-link voltage might increase above this threshold during voltage dip, reaching over 200 V. The system is connected to a 50 Hz, 40 V line-line grid voltage v_{grid} . Grid active power P_{grid} reaches 95 W, while the grid injected current i_{grid} corresponds to 1.4A (2A peak).

The control system and the switching strategy for GSC and the MSC have been implemented using a 32-bit TriCore microcontroller TC1796 from Infineon. Voltage dips were emulated using a coupling, multi-turn step-up transformer connecting the GSC to the grid through the primary side.

Due to the limited power level of the experimental test rig, the moment of inertia of the experimental prototype is lower than that of the simulated system. As a result, the rotor speed might cross the overspeed limit during the sag. Therefore, the fault duration is adjusted to 60 msec to avoid PMSG speed increase while keeping same depth of the voltage dip (70%) and thus validating the proposed technique concept.

Experimental results for the proposed technique have been compared to the results obtained with the conventional non-swap control action as shown in Figures 13 and 14. Table 5 summarizes experimental performance results during the 70% grid voltage dip.

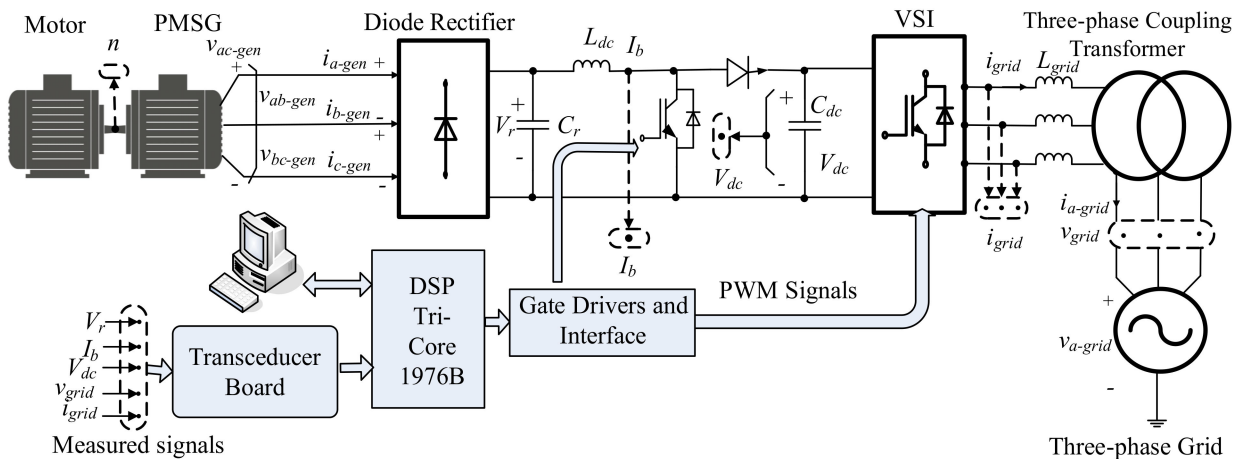


Figure 11. Block diagram of experimental set-up.

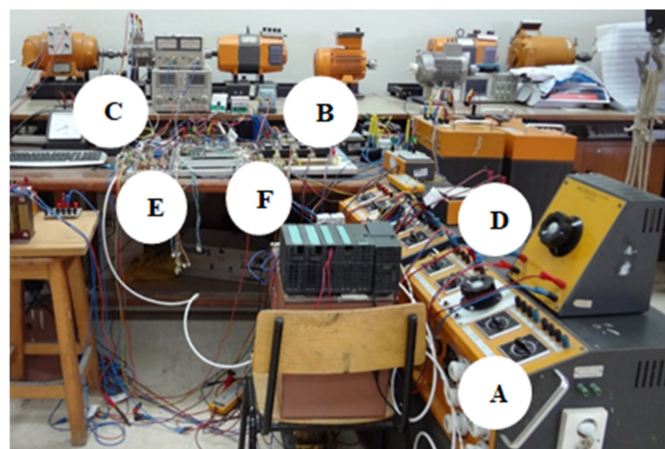


Figure 12. Photograph of the experimental prototype: (A) coupling transformer; (B) power converters; (C) prime mover and PMSG; (D) grid side and filter; (E) voltage and current transducer boards; (F) DSP Tri-core 197.

Table 4. Experimental set-up parameters.

| Variable | Parameter | Value |
|-------------|--|-------|
| P_{gen} | Rated power (kW) | 0.31 |
| R_a | Stator Resistance (Ω) | 12.5 |
| φ_f | Field Flux linkage | 0.36 |
| J | Moment of Inertia (kg.m^2) | 0.016 |
| v_{gen} | Nominal Voltage at 1500 rpm (V) | 200 |
| P | Number of poles | 4 |
| f_c | PWM switching frequency (Hz) | 5000 |
| L_{dc} | Boost converter inductance (mH) | 10 |
| C_r | Input boost converter capacitor (μF) | 1200 |
| C_{dc} | DC-link capacitor (μF) | 2200 |
| V_{dc} | DC-link reference voltage (V) | 100 |
| v_{grid} | Line-line grid voltage (V) | 40 |
| L | Grid filter and coupling transformer inductance (mH) | 2 |
| R | Grid filter and coupling transformer resistance (Ω) | 1.5 |
| f_{grid} | Grid frequency (Hz) | 50 |

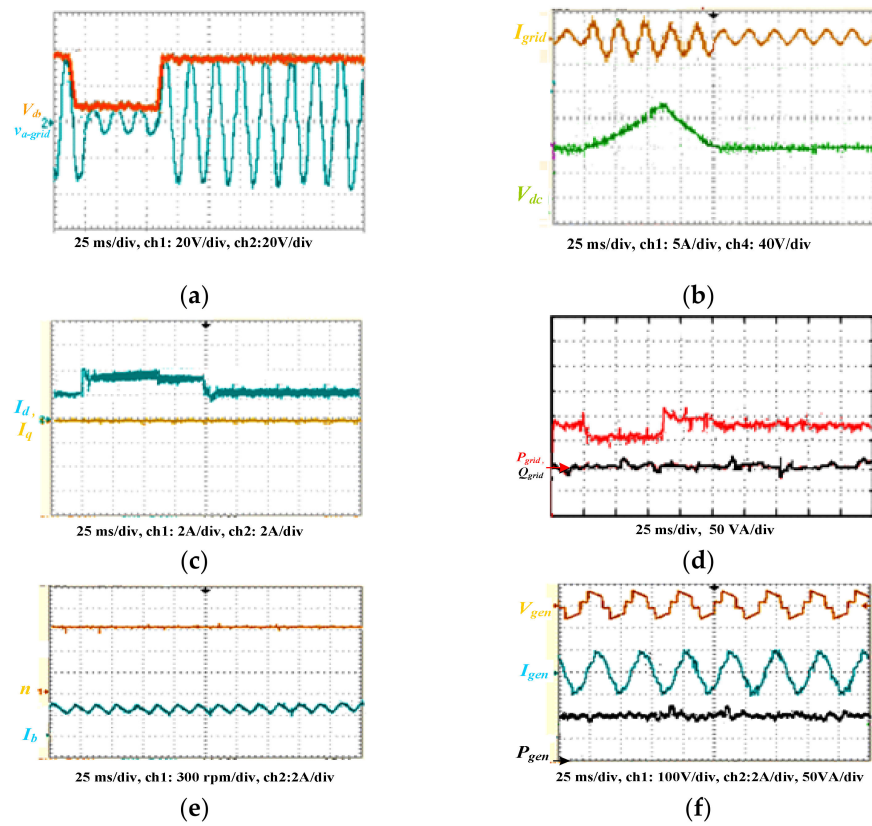


Figure 13. Experimental results during 70% symmetrical grid voltage dip without the proposed control scheme: (a) phase ‘a’ grid voltage v_{grid} and d-axis grid voltage V_d ; (b) phase ‘a’ grid current i_{grid} and DC-link voltage V_{dc} ; (c) d- and q-axis grid currents I_d and I_q ; (d) grid active power P_{grid} and reactive power Q_{grid} ; (e) Boost chopper current I_b and PMSG speed n ; (f) PMSG Line-line voltage v_{ab-gen} , phase a-current i_{a-gen} and active power P_{gen} .

Using the proposed control technique, the DC-link voltage V_{dc} is preserved at a constant value to 100 V, while phase a-grid current i_{a-grid} at 1.4A (2A peak), during the dip, compared to $V_{dc} = 160$ V and $i_{a-grid} = 2.8$ A (4A peak) without the suggested control as shown in Figures 13b and 14b, respectively. This DC-link rise is successfully limited for converters’ safety; in addition, grid currents are maintained within their nominal value during normal and LVRT operation. Since the voltage sag is less than 50%, $I_d = 0$, $I_q = 2A$ during the dip when applying the proposed technique resulting in $P_{grid} = 0$, $Q_{grid} = 30$ W compared to the values of $P_{grid} = 60$ W, $Q_{grid} = 0$ VAR without the proposed technique. Since MPPT is terminated in the proposed technique, boost inductor current I_b changes from $I_b = 2A$ to $I_b = 0$, and generator current becomes $i_{a-gen} = 0$; thus, the generator active

power P_{gen} will be zero. The shaft mechanical speed n increases from 900 to approximately 1012 rpm with the suggested control technique, equivalent to 1.1 p.u.

After the dip is cleared, the MSC recovers back the PMSG speed while the GSC retakes the charge of the DC-link voltage. Energy stored in the rotor inertia during the dip incident is being released into the grid while the generator and grid currents reach their pre-fault values.

Experimental grid current results, for both cases (swap and non-swap schemes) are analyzed during LVRT as shown in Figure 15. Grid current THD is enhanced during LVRT from 12% with the non-swap scheme to 5% using swap control. This confirmed the ability of the swap to decouple the DC-link voltage control dynamics from the grid current one during LVRT, thus enhancing THD during fault.

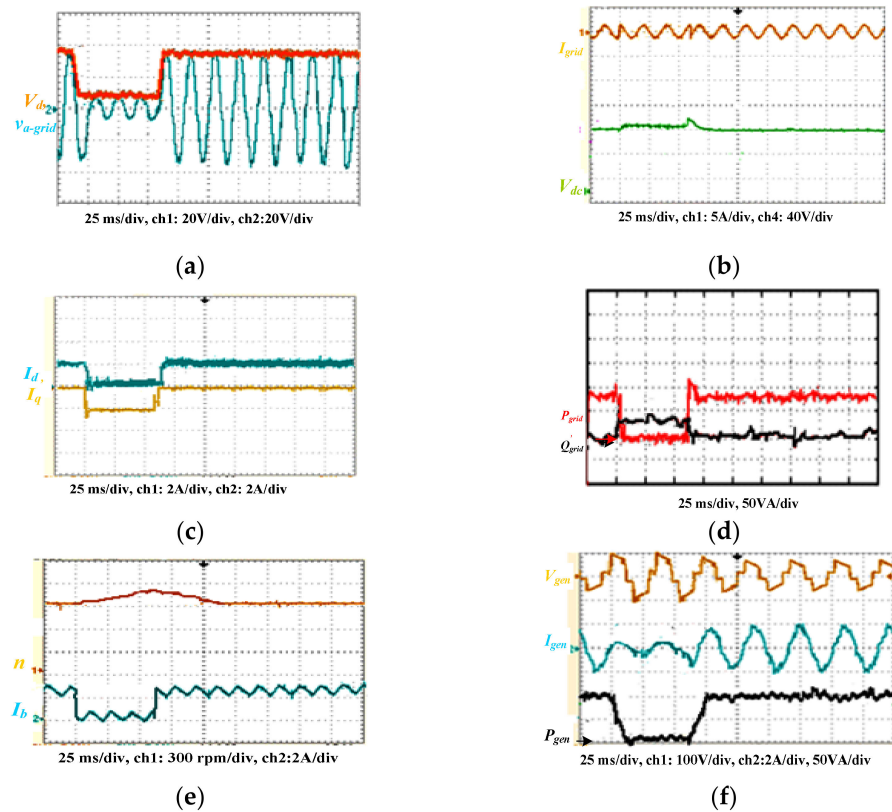


Figure 14. Experimental results during 70% symmetrical grid voltage dip using the proposed control scheme: (a) phase ‘a’ grid voltage v_{grid} and d– axis grid voltage V_d ; (b) phase ‘a’ grid current i_{grid} and DC– link voltage V_{dc} ; (c) dq– axis grid currents I_d and I_q ; (d) grid active power P_{grid} and reactive power Q_{grid} ; (e) Boost chopper current I_b and PMSG speed n ; (f) PMSG Line-line voltage v_{ab-gen} , phase a– current i_{a-gen} and active power P_{gen} .

Table 5. Experimental performance results.

| Results During Fault | During 70% Voltage Sag | |
|----------------------|------------------------|-------------------------|
| | No Mode-Shift Control | With Mode-Shift Control |
| I_b (A) | 2 | 0 |
| I_d (A) | 4 | 0 |
| I_q (A) | 0 | −2 |
| $I_{grid, peak}$ (A) | 4 | 2 |
| %THD | 12% | 5% |
| V_{dc} (V) | 160 | 100 |
| P_{grid} (W) | 60 | 0 |
| Q_{grid} (W) | 0 | 30 |

Good agreement can be found between the simulated system results and those of the correlated experimental prototype, which verifies the proposed approach's effectiveness.

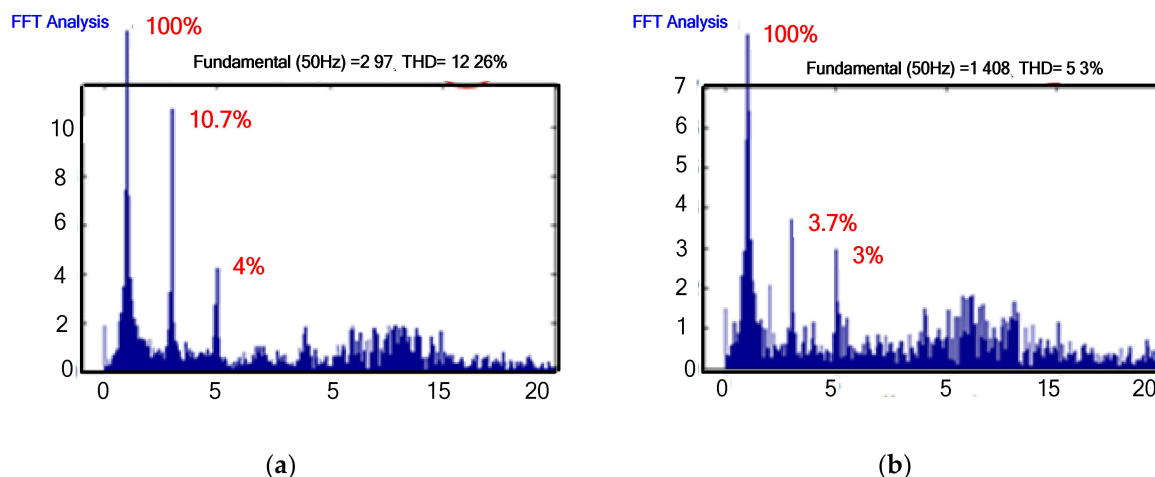


Figure 15. FFT analysis of experimental grid current during 70% LVRT for (a) non-swap control and (b) swap control.

7. Discussion

At present, DFIG and PMSG are two mainstays of wind turbine generators that dominate the energy market. However, the PMSG option facilitates the elimination of the gearbox, which is easily broken. Besides featuring high energy conversion efficiency compared to other types at low maintenance costs, PMSG WECS offer high-power density and complete active and reactive power control. However, these features are met at the cost of larger and heavier generators. For grid integration, PMSG are employed with full-scale power converters that feature isolation from grid disturbances, thus adding robustness to their fault ride through capabilities. Hence, the PMSG-based WECS is considered in this paper. In [49], a review on commercialized drivetrain system technologies of wind turbines is performed. It was found that direct driven PMSG is the dominant technology of Siemens Gamesa and GE for fixed/floating offshore platforms.

PMSG power converters must be sized at the full-scale rating of the generator capacity, thus adding cost and size to the overall system. To manage the trade-off between the PMSG fault tolerance capabilities and its high converter cost, the PMSG WECS considered in this paper applies an economic converter topology rather than the traditional back-to-back one. The considered converter topology is a passive front-end converter (diode rectifier) assisted with a DC/DC boost converter for the MSC stage and a three-phase VSI as the GSC stage. The considered MSC topology features seven passive switches with only one active switch and one gate-driver, compared to the classical active front-end topology featuring six active switches and six gate-drive circuits. Thus, the considered MSC converter size and cost are reduced as well as its implementation and control complexity. Besides, less switching losses are exhibited, especially at low and average turbine speeds, making it a predominant solution for low and medium power ranges. However, this is achieved at the cost of higher generator torque ripples and generator current harmonics, as this converter experiences limited generator-side control.

To achieve a fault-tolerant PMSG-based WECS featuring efficient LVRT, a swap control feature is proposed to modify the classical converters' control scheme during voltage dips. During LVRT mode, the proposed modification shifts the role of DC-link voltage regulation to be overtaken by the MSC independently of the grid current control and VAR support achieved by the GSC. This feature has the following benefits. First, the MPPT is seized, and only adequate wind power is extracted by the MSC sufficient to maintain DC-link nominal voltage level and prevent any rises. Second, the VSI prime focus is VAR injection instead of performing two control functions. VAR injection is achieved according to dip depth

at fast dynamics, which is totally independent from the slow dynamic V_{dc} control. Third, computing the grid current's d -component from the $I_d - I_q$ relation, rather than from the affected DC-link voltage loop, improves grid current THD as well as fastens grid current control dynamics. Fourth, the proposed swap enhancement is quite flexible since it can be implemented on the existing systems without any hardware modifications. It is applicable to any existing WECS involving full-rated converters such as synchronous generator-based WECS, which are the considered systems in this research. Finally, any rises in DC-link voltage or grid current during dips, due to energy mismatch, are mitigated by storing any surplus energy in rotor inertia without needing an extra hardware device, which adds to system cost-effectiveness.

At voltage dips, using the proposed swap control, VAR injection for grid support reduces the amount of transferrable active grid power, following Equations (36)–(38). Thus, the grid current is maintained within the system nominal values for safe power converters' operation. However, power imbalance occurs due to the mismatch between the generator shaft mechanical torque T_m and its electromagnetic developed torque T_e as per the synchronous generator swing equation demonstrated in (39) [50]:

$$T_m - T_e = T_a = J \omega_{gen} \quad (39)$$

where T_a is the rotor accelerating torque, J is the moment of inertia and ω_{gen} is the generator angular speed of rotation. Hence, energy mismatch and speed deviation can be represented by (40):

$$(P_m - P_e)dt = \frac{1}{2} J (\omega_{gen, fault}^2 - \omega_{gen, rated}^2) \quad (40)$$

where P_m is the generator input mechanical power ignoring the rotational losses, P_e is the generator electrical output power ignoring electrical losses, $\omega_{gen, rated}$ is the rated generator speed (before fault occurrence), $\omega_{gen, fault}$ is the shaft speed during fault and t_{fault} is the fault duration in msec [35,51].

Assuming maximum energy mismatch when $P_{grid} \approx 0$ (grid voltage dip < 50%), the maximum generator speed during fault $\omega_{gen, max}$ can be calculated using (41):

$$\omega_{gen, max} = \sqrt{\frac{2P_{gen}t_{fault}}{J} + \omega_{gen, rated}^2} \quad (41)$$

For simulation work, the value of fault duration t_{fault} is set to 150 msec, corresponding to the maximum permissible fault duration without tripping the wind turbine as per the Eon-Netz grid code requirements shown in Figure 1a. Thus, theoretically, for the considered 1.5 MW turbine, combined mechanical system inertia is chosen as $J = 5 \text{ Mkgm}^2$ [52]. Given that $\omega_{gen, rated} = 1.8 \text{ rad/s}$, the expression (41) gives $\omega_{gen, max} = 1.824 \text{ rad/s}$ corresponding to 1.24 rad/s and a speed increase of 0.24 rpm. Using these values, it is noted that the PMSG speed increase is 1.36% above the rated value owing to the inherent characteristic of the large turbine and generator inertia. These results demonstrate that the concept of storing energy in the rotating mass can be applied to real WECS. Compared to other energy storage techniques, no power is being dissipated as in the chopper-controlled crowbar method and no additional hardware is needed as in systems that use super capacitors or batteries [51].

In addition, the stored energy during the fault can be injected once again to the grid upon grid voltage recovery. Moreover, it is a safe approach since most commercial wind turbines are equipped with an overspeed capability, which offers overspeed protection at 130% above nominal speed [7]. It is worth mentioning that the above calculations depend on the grid dip profile and length, i.e., if the fault duration is too long, the generator may cross the overspeed capability limit. If this scenario happens, pitch mechanism can be employed to trip the turbine.

For the correlated experimental prototype and using the experimental values found in Table 4, similar calculations' procedure yields to $\omega_{gen,max} = 105.5$ rad/s when t_{fault} is set to 60 msec compared to $\omega_{gen,rated} = 94.24$ rad/s. Thus, the speed increase is 107.45 rpm corresponding to 10.66% increase, which is still within machine-safe speed limits.

To sum up, Table 6 compares the features of the considered PMSG versus the popular DFIG one. Moreover, it lists merits and limitations of the applied MSC topology, versus the popular active front-end one, as well as showing the superiority of the proposed swap control. Finally, simulation-set-up results as well as those of the correlated experimental prototype verify the effectiveness of the proposed swap scheme.

Table 6. Comparison between the considered WECS components and applied control versus those of classical WECS systems [3–10].

| | Generator Type | |
|---|---|--|
| | DFIG | PMSG |
| Components' limitations | Gear box and slip rings (require more maintenance) | Multi-pole PMSG (heavy and big) |
| Reliability | Less | More |
| Failure rate | More | Less |
| VAR and P control | Partial control | Complete control |
| LVRT capability | Less | More |
| Converter capacity | Partial power converter | Full power converter |
| Converter size and cost | less | More |
| | MSC | |
| | Active front-end | Passive front-end+ boost chopper |
| Active switches and gate drives number | More | Less |
| Size and cost | More | Less |
| Implementation complexity | More | Less |
| Control complexity | More | Less |
| Switching losses at low and medium speeds | More | Less |
| Switching losses at high speeds | Less | More |
| Generator-side control | Full | Limited |
| Generator torque ripples and noise | Less | More |
| Generator current harmonics | Less | More |
| | Action during LVRT | |
| | Non-swap | Swap |
| MSC | MPPT | Seize MPPT DC-link voltage regulation |
| GSC | DC-link voltage regulation and grid current d -component control | Grid current d and q components' control |
| Decouple between V_{dc} and I_{grid} dynamics | No | Yes |
| VAR injection | No | Yes |
| Surplus energy | In DC-link causing V_{dc} and I_{grid} increases, otherwise extra hardware device is required | In rotor inertia with no need of extra hardware mitigating V_{dc} and I_{grid} rises |

8. Conclusions

This paper introduces a cost-effective WECS featuring efficient LVRT capability via a proposed modification to the classical control technique without adding any auxiliary hardware devices. The PMSG is addressed rather than DFIG due to its superior fault tolerance capabilities. However, the PMSG-based WECS requires a full-power converter topology, which makes it an expensive alternative. To compensate for this tradeoff, a passive front-end rectifier assisted by a boost chopper is used as the MSC followed by a three-phase current-controlled VSI as the GSC. This topology is employed rather than the popular back-to-back topology since the former topology is assisted with fewer active switches, gate drive circuits and switching losses, especially at low and average wind speeds. Thus, converter cost, size, and implementation and control complexity are reduced, making it a favorable solution for low and medium power ranges and for distant WES generators. However, these merits are achieved at the cost of higher torque pulsations and noise.

During voltage dips, the mode-shift (swap) LVRT feature, proposed in this paper, maintains the DC-link voltage and grid currents at safe boundaries without any need for additional hardware requirement. Moreover, it decouples the DC-link voltage control from grid current control during faults, which adds to system robustness. This modification serves the main objective of achieving an economic fault-tolerant flexible fault-ride-through solution applicable for existing or future PMSG-WECS. Besides, any energy surplus is stored in the rotor inertia; thus, the proposed approach is most favorable for MW direct-driven PMSG wind turbines, which possess a large moment of inertia

Simulation results of the considered 1.5 MW PMSG-based system, under 70% voltage dip, verified the superiority of the proposed swap approach over the classical non-swap one. Comparatively, the former was able to mitigate a 20% rise in grid current and DC-link voltage nominal values. Moreover, grid current THD is reduced from 6% using the non-swap control to 3% using the proposed swap one. The simulation set-up was correlated to an experimental prototype and tested for the same circumstances. The proposed swap control was able to mitigate a 60% rise in V_{dc} and almost a 100% rise in grid current as well as reduce the THD from 12% to 5% during a 70% voltage dip. Thus, the simulation and experimental results verified the effectiveness of the proposed approach during normal and LVRT operation modes.

9. Future Work

For enhancing the considered WECS performance, authors may wish to address unsymmetrical grid faults and wind energy generator disturbances in future work.

Author Contributions: Investigation, R.A.I. and N.E.Z.; Methodology, R.A.I. and N.E.Z.; Software, N.E.Z.; Validation, R.A.I.; Writing—original draft, R.A.I.; Writing—review & editing, N.E.Z. All authors have read and agreed to the published version of the manuscript.

Funding: This research received no external funding.

Informed Consent Statement: Not applicable.

Conflicts of Interest: The authors declare no conflict of interest.

Nomenclature

The following abbreviations are used in this manuscript:

| | |
|------|---|
| AFER | Active front-end rectifier |
| DFIG | Double fed induction generator |
| FACT | Flexible AC transmission devices |
| GSC | Grid-side converter |
| LVRT | Low-voltage ride-through |
| MPPT | Maximum power point tracking |
| MSC | Machine-side converter |
| ORB | Optimum relationship-based control |
| PCC | Point of common coupling |
| PLL | Phase-lock loop |
| PMSG | Permanent magnet synchronous generators |
| SPWM | Sinusoidal pulse width modulation |
| SW | Switch |
| SW1 | Boost converter switch |
| THD | Total harmonic distortion |
| VSI | Voltage source inverter |
| WECS | Wind energy conversion systems |

The following symbols are used in this manuscript:

| | |
|---------------------------------|--|
| A | Blades swept area, m^2 |
| C_{dc} | DC-link capacitor, F |
| C_r | Rectifier output filter capacitor, F |
| C_p | Power coefficient |
| d | Boost converter duty ratio |
| I_N | Normal grid current, A |
| $i_{abc-gen}$ | 3-phase stator currents, A |
| I_b^*, I_b | Chopper inductor current reference and actual, respectively, A |
| I_d^*, I_d | Reference and actual active grid current, respectively, A |
| i_{grid} | 3-phase grid currents, A |
| i_{dc} | VSI instantaneous input DC current, A |
| J | Moment of inertia, kg/m^2 |
| L | Grid inductance, H |
| L_{dc} | Boost chopper inductance, H |
| L_{dq} | Generator dq axis stator inductance, H |
| m | Inverter modulation index |
| P_{r-opt}, P_{MPP} | Optimal rectifier output power and peak power, respectively, W |
| P_{grid} | Active grid power W, |
| P_{gen} | Active generator power W, |
| P_m | Mechanical shaft power, W |
| P_w | Extracted power by wind turbine, W |
| Q_{gen} | reactive generator power, VAR |
| Q_{grid} | Reactive grid power, VAR |
| r | Windmill blade radius, m |
| R | Grid resistance, Ω |
| R_a | Stator windings resistance/phase, Ω |
| T_e, T_L, T_a | Electromechanical, load and accelerating torque, Nm |
| V_r, V_{r-opt} | Rectifier output voltage and optimal value, respectively, V |
| $V_{dc}, v_{dc}, \Delta v_{dc}$ | DC-link capacitor voltage, instantaneous and voltage ripple, respectively, V |
| V_d^*, V_d | Reference and actual d-axis grid voltage, respectively, V |
| $(\hat{V}_{LLinv})_{max}$ | Maximum amplitude of the line-to-line inverter voltage, V |
| V_{PCC} | Point of common coupling voltage, V |
| V_q^*, V_q | Reference and actual reactive grid voltage, respectively, V |
| $v_{abc-grid}$ | Phase-to-neutral grid voltages, V |
| $v_{dq0-gen}$ | Generator voltages in $dq0$ rotating reference frame, V |
| v_{grid} | 3-phase grid voltages, V |
| v_{inv} | VSI output AC voltage, V |
| Δi_b | Boost inductor current ripple |
| β, ω, λ | Pitch blades angle $^\circ$, blade tip speed m/s, tip speed ratio |
| ρ, V_W | Wind density kg/m^3 , wind speed, m/s |
| φ_f | Permanent magnet flux linkage, V/rad/s |
| ω_{gen} | Generator angular speed, rad/s |
| ω_r, ω_s | PMSG rotor angular and electrical velocity, respectively, rad/s |

References

1. REN21, R. Global Status Report. Available online: <https://www.ren21.net/reports/global-status-report/> (accessed on 1 December 2021).
2. GWEC. Global Wind Report. Available online: <https://gwec.net/global-wind-report-2021/> (accessed on 1 December 2021).
3. Nejad, A.R.; Keller, J.; Guo, Y.; Sheng, S.; Polinder, H.; Watson, S.; Dong, J.; Qin, Z.; Ebrahimi, A.; Schelenz, R.; et al. Wind turbine drivetrains: State-of-the-art technologies and future development trends. *Wind Energ. Sci. Discuss.* **2021**, *2021*, 1–35. [CrossRef]
4. Vijayaprabhu, A.; Bhaskar, K.B.; Jasmine Susila, D.; Dinesh, M. Review and Comparison of Various Types of Generation Using WECS Topologies. *IOP Conf. Ser. Mater. Sci. Eng.* **2021**, *1177*, 012004. [CrossRef]
5. Carroll, J.; McDonald, A.; McMillan, D. Reliability Comparison of Wind Turbines with DFIG and PMG Drive Trains. *IEEE Trans. Energy Convers.* **2015**, *30*, 663–670. [CrossRef]
6. Yaramasu, V.; Wu, B.; Sen, P.C.; Kouro, S.; Narimani, M. High-power wind energy conversion systems: State-of-the-art and emerging technologies. *Proc. IEEE* **2015**, *103*, 740–788. [CrossRef]

7. Yaramasu, V.; Wu, B.; Alepuz, S.; Kouro, S. Predictive Control for Low-Voltage Ride-Through Enhancement of Three-Level-Boost and NPC-Converter-Based PMSG Wind Turbine. *IEEE Trans. Ind. Electron.* **2014**, *61*, 6832–6843. [[CrossRef](#)]
8. Rahimi, M. Modeling, control and stability analysis of grid connected PMSG based wind turbine assisted with diode rectifier and boost converter. *Int. J. Electr. Power Energy Syst.* **2017**, *93*, 84–96. [[CrossRef](#)]
9. Sikorski, A.; Falkowski, P.; Korzeniewski, M. Comparison of Two Power Converter Topologies in Wind Turbine System. *Energies* **2021**, *14*, 6574. [[CrossRef](#)]
10. Yaramasu, V.; Dekka, A.; Durán, M.J.; Kouro, S.; Wu, B. PMSG-based wind energy conversion systems: Survey on power converters and controls. *IET Electr. Power Appl.* **2017**, *11*, 956–968. [[CrossRef](#)]
11. Mahela, O.P.; Gupta, N.; Khosravy, M.; Patel, N. Comprehensive Overview of Low Voltage Ride through Methods of Grid Integrated Wind Generator. *IEEE Access* **2019**, *7*, 99299–99326. [[CrossRef](#)]
12. Ibrahim, R.A.; Hamad, M.S.; Dessouky, Y.G.; Williams, B.W. A review on recent low voltage ride-through solutions for PMSG wind turbine. In Proceedings of the International Symposium on Power Electronics Power Electronics, Electrical Drives, Automation and Motion, Sorrento, Italy, 20–22 June 2012; pp. 265–270.
13. Nasiri, M.; Mobayen, S.; Faridpak, B.; Fekih, A.; Chang, A. Small-Signal Modeling of PMSG-Based Wind Turbine for Low Voltage Ride-Through and Artificial Intelligent Studies. *Energies* **2020**, *13*, 6685. [[CrossRef](#)]
14. Nasiri, M.; Milimonfared, J.; Fathi, S.H. A review of low-voltage ride-through enhancement methods for permanent magnet synchronous generator based wind turbines. *Renew. Sustain. Energy Rev.* **2015**, *47*, 399–415. [[CrossRef](#)]
15. Jahanpour-Dehkordi, M.; Vaez-Zadeh, S.; Mohammadi, J. Development of a Combined Control System to Improve the Performance of a PMSG-Based Wind Energy Conversion System Under Normal and Grid Fault Conditions. *IEEE Trans. Energy Convers.* **2019**, *34*, 1287–1295. [[CrossRef](#)]
16. Luo, X.; Wang, J.; Wojcik, J.D.; Wang, J.; Li, D.; Draganescu, M.; Li, Y.; Miao, S. Review of Voltage and Frequency Grid Code Specifications for Electrical Energy Storage Applications. *Energies* **2018**, *11*, 1070. [[CrossRef](#)]
17. Mendes, V.F.; Matos, F.F.; Liu, S.Y.; Cupertino, A.F.; Pereira, H.A.; De Sousa, C.V. Low Voltage Ride-Through Capability Solutions for Permanent Magnet Synchronous Wind Generators. *Energies* **2016**, *9*, 59. [[CrossRef](#)]
18. Zhong, C.; Wei, L.; Yan, G. Low Voltage Ride-through Scheme of the PMSG Wind Power System Based on Coordinated Instantaneous Active Power Control. *Energies* **2017**, *10*, 995. [[CrossRef](#)]
19. Yan, X.; Yang, L.; Li, T. The LVRT Control Scheme for PMSG-Based Wind Turbine Generator Based on the Coordinated Control of Rotor Overspeed and Supercapacitor Energy Storage. *Energies* **2021**, *14*, 518. [[CrossRef](#)]
20. Kim, C.; Kim, W. Low-Voltage Ride-Through Coordinated Control for PMSG Wind Turbines Using De-Loaded Operation. *IEEE Access* **2021**, *9*, 66599–66606. [[CrossRef](#)]
21. Xing, P.; Fu, L.; Wang, G.; Wang, Y.; Zhang, Y. A composite control method of low-voltage ride through for PMSG-based wind turbine generator system. *IET Gener. Transm. Distrib.* **2018**, *12*, 117–125. [[CrossRef](#)]
22. Abdelrahem, M.; Kennel, R. Fault-Ride through Strategy for Permanent-Magnet Synchronous Generators in Variable-Speed Wind Turbines. *Energies* **2016**, *9*, 1066. [[CrossRef](#)]
23. Nasiri, M.; Mohammadi, R. Peak Current Limitation for Grid Side Inverter by Limited Active Power in PMSG-Based Wind Turbines During Different Grid Faults. *IEEE Trans. Sustain. Energy* **2017**, *8*, 3–12. [[CrossRef](#)]
24. Alotaibi, I.; Abido, M.A.; Khalid, M.; Savkin, A.V. A Comprehensive Review of Recent Advances in Smart Grids: A Sustainable Future with Renewable Energy Resources. *Energies* **2020**, *13*, 6269. [[CrossRef](#)]
25. Gmbh, E.O.N. Grid Code- High and Extra High Voltage. Available online: http://www.pvupscale.org/IMG/pdf/D4_2_DE_annex_A-3_EON_HV_grid_connection_requirements_ENENARHS2006de.pdf (accessed on 1 December 2021).
26. Mahrouch, A.; Ouassaid, M.; Elyaaloui, K. LVRT Control for Wind Farm Based on Permanent Magnet Synchronous Generator Connected into the Grid. In Proceedings of the 2017 International Renewable and Sustainable Energy Conference (IRSEC), Tangier, Morocco, 4–7 December 2017; pp. 1–6.
27. Zhou, A.; Li, Y.W.; Mohamed, Y. Mechanical Stress Comparison of PMSG Wind Turbine LVRT Methods. *IEEE Trans. Energy Convers.* **2021**, *36*, 682–692. [[CrossRef](#)]
28. Saadat, N.; Choi, S.S.; Vilathgamuwa, D.M. A Statistical Evaluation of the Capability of Distributed Renewable Generator-Energy-Storage System in Providing Load Low-Voltage Ride-Through. *IEEE Trans. Power Deliv.* **2015**, *30*, 1128–1136. [[CrossRef](#)]
29. Huang, C.; Zheng, Z.; Xiao, X.; Chen, X. Enhancing low-voltage ride-through capability of PMSG based on cost-effective fault current limiter and modified WTG control. *Electr. Power Syst. Res.* **2020**, *185*, 106358. [[CrossRef](#)]
30. Geng, H.; Liu, L.; Li, R. Synchronization and Reactive Current Support of PMSG-Based Wind Farm During Severe Grid Fault. *IEEE Trans. Sustain. Energy* **2018**, *9*, 1596–1604. [[CrossRef](#)]
31. Dey, P.; Datta, M.; Fernando, N.; Senju, T. Fault-ride-through performance improvement of a PMSG based wind energy systems via coordinated control of STATCOM. In Proceedings of the 2018 IEEE International Conference on Industrial Technology (ICIT), Lyon, France, 20–22 February 2018; pp. 1236–1241.
32. Yunus, A.M.S.; Abu-Siada, A.; Masoum, M.A.S.; El-Naggar, M.F.; Jin, J.X. Enhancement of DFIG LVRT Capability During Extreme Short-Wind Gust Events Using SMES Technology. *IEEE Access* **2020**, *8*, 47264–47271. [[CrossRef](#)]
33. Ghany, A.A.; Shehata, E.G.; Elsayed, A.-H.M.; Mohamed, Y.S.; Haes Alhelou, H.; Siano, P.; Diab, A.A.Z. Novel Switching Frequency FCS-MPC of PMSG for Grid-Connected Wind Energy Conversion System with Coordinated Low Voltage Ride Through. *Electronics* **2021**, *10*, 492. [[CrossRef](#)]

34. Basak, R.; Bhuvanewari, G.; Pillai, R.R. Low-Voltage Ride-Through of a Synchronous Generator-Based Variable Speed Grid-Interfaced Wind Energy Conversion System. *IEEE Trans. Ind. Appl.* **2020**, *56*, 752–762. [[CrossRef](#)]
35. Alepuz, S.; Calle, A.; Busquets-Monge, S.; Kouro, S.; Wu, B. Use of Stored Energy in PMSG Rotor Inertia for Low-Voltage Ride-Through in Back-to-Back NPC Converter-Based Wind Power Systems. *IEEE Trans. Ind. Electron.* **2013**, *60*, 1787–1796. [[CrossRef](#)]
36. Boersma, S.; Doekemeijer, B.M.; Gebraad, P.M.O.; Fleming, P.A.; Annoni, J.; Scholbrock, A.K.; Frederik, J.A.; Wingerden, J.W.V. A tutorial on control-oriented modeling and control of wind farms. In Proceedings of the 2017 American Control Conference (ACC), Seattle, WA, USA, 24–26 May 2017; pp. 1–18.
37. Azer, P.; Emadi, A. Generalized State Space Average Model for Multi-Phase Interleaved Buck, Boost and Buck-Boost DC-DC Converters: Transient, Steady-State and Switching Dynamics. *IEEE Access* **2020**, *8*, 77735–77745. [[CrossRef](#)]
38. Steady state and averaged state space modelling of non-ideal boost converter. *Int. J. Power Electron.* **2015**, *7*, 109–133. [[CrossRef](#)]
39. Chaudhuri, N.R.; Lee, C.K.; Chaudhuri, B.; Hui, S.Y.R. Dynamic Modeling of Electric Springs. *IEEE Trans. Smart Grid* **2014**, *5*, 2450–2458. [[CrossRef](#)]
40. Khamis, A.K.; Zakzouk, N.E.; Abdelsalam, A.K.; Lotfy, A.A. Decoupled Control Strategy for Electric Springs: Dual Functionality Feature. *IEEE Access* **2019**, *7*, 57725–57740. [[CrossRef](#)]
41. Blaabjerg, F.; Teodorescu, R.; Liserre, M.; Timbus, A.V. Overview of Control and Grid Synchronization for Distributed Power Generation Systems. *IEEE Trans. Ind. Electron.* **2006**, *53*, 1398–1409. [[CrossRef](#)]
42. Hamadi, A.; Rahmani, S.; Ndtoungou, A.; Al-Haddad, K.; Kanaan, H.Y. A new Maximum Power Point Tracking with indirect current control for a three-phase grid-connected inverter used in PMSG-based wind power generation systems. In Proceedings of the IECON 2012-38th Annual Conference on IEEE Industrial Electronics Society, Montreal, QC, Canada, 25–28 October 2012; pp. 916–923.
43. Li, S.; Haskew, T.A.; Swatloski, R.P.; Gathings, W. Optimal and Direct-Current Vector Control of Direct-Driven PMSG Wind Turbines. *IEEE Trans. Power Electron.* **2012**, *27*, 2325–2337. [[CrossRef](#)]
44. Chen, W.; Zheng, T.; Han, J. Fault Characteristic and Low Voltage Ride-Through Requirements Applicability Analysis for a Permanent Magnet Synchronous Generator-Based Wind Farm. *Energies* **2019**, *12*, 3400. [[CrossRef](#)]
45. Abdullah, M.A.; Yatim, A.H.M.; Tan, C.W. An online optimum-relation-based maximum power point tracking algorithm for wind energy conversion system. In Proceedings of the 2014 Australasian Universities Power Engineering Conference (AUPEC), Perth, Australia, 28 September–1 October 2014; pp. 1–6.
46. Chen, Z.; Yin, M.; Zou, Y.; Meng, K.; Dong, Z. Maximum Wind Energy Extraction for Variable Speed Wind Turbines With Slow Dynamic Behavior. *IEEE Trans. Power Syst.* **2017**, *32*, 3321–3322. [[CrossRef](#)]
47. Xia, Y.; Ahmed, K.H.; Williams, B.W. A New Maximum Power Point Tracking Technique for Permanent Magnet Synchronous Generator Based Wind Energy Conversion System. *IEEE Trans. Power Electron.* **2011**, *26*, 3609–3620. [[CrossRef](#)]
48. Yang, Y.; Blaabjerg, F. Low-Voltage Ride-Through Capability of a Single-Stage Single-Phase Photovoltaic System Connected to the Low-Voltage Grid. *Int. J. Photoenergy* **2013**, *2013*, 257487. [[CrossRef](#)]
49. Moghadam, F.K.; Nejad, A.R. Evaluation of PMSG-based drivetrain technologies for 10-MW floating offshore wind turbines: Pros and cons in a life cycle perspective. *Wind Energy* **2020**, *23*, 1542–1563. [[CrossRef](#)]
50. Qais, M.H.; Hasanien, H.M.; Alghuwainem, S. A Grey Wolf Optimizer for Optimum Parameters of Multiple PI Controllers of a Grid-Connected PMSG Driven by Variable Speed Wind Turbine. *IEEE Access* **2018**, *6*, 44120–44128. [[CrossRef](#)]
51. Fernández-Bustamante, P.; Barambones, O.; Calvo, I.; Napole, C.; Derbeli, M. Provision of Frequency Response from Wind Farms: A Review. *Energies* **2021**, *14*, 6689. [[CrossRef](#)]
52. Knudsen, H.; Nielsen, J.N. Introduction to the Modelling of Wind Turbines. In *Wind Power in Power Systems*; Wiley: Chichester, UK, 2005; pp. 523–554.